VACUUM METROLOGY AND THE ROLE OF SURFACE CONDITIONS ON THE TANGENTIAL MOMENTUM ACCOMMODATION OF MOLECULES IN A RAREFIED GAS

Tim Verbovšek

Doctoral Dissertation
Jožef Stefan International Postgraduate School
Ljubljana, Slovenia

Supervisor: Dr. Janez Šetina, Institute of Metals and Technology, Ljubljana, Slovenia

Evaluation Board:
Prof. Dr. Uroš Cvelbar, Chair, Jožef Stefan International Postgraduate School and Jožef Stefan Institute, Ljubljana, Slovenia
Prof. Dr. Monika Jenko, Member, Jožef Stefan International Postgraduate School and Institute of Metals and Technology, Ljubljana, Slovenia
doc. RNDr. Jiří Tesař, Member, Czech Metrology Institute (CMI), Brno, Czech Republic

MEDNARODNA PODIPLOMSKA ŠOLA JOŽEFA STEFANA
JOŽEF STEFAN INTERNATIONAL POSTGRADUATE SCHOOL

Tim Verbovšek

VACUUM METROLOGY AND THE ROLE OF SURFACE CONDITIONS ON THE TANGENTIAL MOMENTUM ACCOMMODATION OF MOLECULES IN A RAREFIED GAS

Doctoral Dissertation

VAKUUMSKO MEROSLOVJE IN VLOGA STANJA POVRŠIN NA PRENOS TANGENCIALNE KOMPONENTE GIBALNE KOLIČINE MOLEKUL V RAZREDČENIH PLINIH

Doktorska disertacija

Supervisor: Dr. Janez Šetina

Ljubljana, Slovenia, September 2020

"Sometimes scientists change their minds. New developments cause a rethink. If this bothers you, consider how much damage is being done to the world by people for whom new developments do not cause a rethink."

— Terry Pratchett, *The Science of Discworld*

Acknowledgments

This work was made possible with financial support through grants by the Slovenian Research Agency (DM H017002 and P2-0056).

Firstly, I would like to thank my supervisor, dr. Janez Šetina, for sharing with me his invaluable experience and knowledge of the ins and outs of vacuum systems and vacuum metrology. Without his help and guidance, this work would be a mess.

Also, thanks to Barbara for guiding me through the process of being a young researcher, and to Patricia for being the middlewoman between me and the IPS. Thanks to Marion and Erik for their help with the AFM.

I would like to thank my family for instilling in me a curious mind, which ultimately led to my interest in science. Also, thanks to my friends, for all the burgers, the fun times, and the long D&D sessions. Lastly, thanks to Ina for the support and for being my anchor when life got a little bit too overwhelming.

Abstract

The interactions between gas molecules and a surface strongly affect the behaviour of systems in a large array of research fields, such as vacuum science and metrology, microfluidics, particle physics, and nuclear physics. In this work, focus is given to the momentum accommodation of gas molecules. The parameter used in this work is the effective tangential momentum accommodation coefficient (ETMAC), which is defined as the relative change of a molecule's tangential component of velocity after collision with the surface. Its importance in two applications is explored; the calibration of a vacuum spinning-rotor gauge (SRG) and the gas-flow conductance of tubes.

The SRG is a vacuum gauge operating on the principle of molecular drag. Gas molecules, surrounding a rotating rotor sphere, collide with the rotor's surface, a process which reduces the rotor's angular momentum. The resulting deceleration rate is directly related to the pressure surrounding the rotor. Here, the ETMAC acts as a calibration constant for the SRG and must be accurately determined in order to minimize the measurement uncertainty of the gauge.

Since the value of the ETMAC is gas-dependent, the SRG calibration must be made in all gases that the gauge is to be used with. This calibration process can therefore quickly become time-consuming. Even more complications arise if gas mixtures are to be used. In this work, an attempt to minimize this gas dependence was made by exposing the rotors to various surface treatments. If the gas dependence of the ETMAC can be reduced, the SRG could be calibrated using only one gas, while retaining a small measurement uncertainty for other gases. It was found that the gas dependence of the ETMAC on a surface roughened by acid etching is decreased with six pure gases; helium, methane, neon, nitrogen, argon, and krypton. The largest deviation from the average value of the ETMAC was observed with helium and neon, the lightest noble gases. Excluding these two gases, however, shows that gas dependence on a roughened surface is about two times lower compared to a polished surface, for the other four gases.

The same gas dependence was explored for the case of the conductance of a long stainless-steel tube. In the molecular flow regime, the number density of the gas molecules is so low that they pass through the tube with a negligible probability of colliding with each other. All collisions therefore occur with the surface. The ETMAC therefore plays an important part in the conductance of such a tube.

For this purpose, a novel method of measuring conductance was developed. It allowed us to determine the conductance, and from it the ETMAC, by using only one pressure gauge. An added advantage is that this pressure gauge does not need to be calibrated, if it has a linear response. The measurement uncertainty of the ETMAC values obtained with this method was below 0.5 %.

In contrast to the rotors of the SRG, it was found that by roughening the surface of the tube with acid etching, the gas dependence could be lowered even for the lightest gases: helium and neon. The spread of ETMAC values for all gases on the roughened surface of the tube was found to be about five times lower than on the polished tube.

Povzetek

Interakcije med molekulami plinov ter površinami močno vplivajo na obnašanje sistemov v številnih področjih raziskav, kot so vakuumska znanost in metrologija, mikrofluidika, fizika delcev ter jedrska fizika. V tem delu smo se osredotočili na akomodacijo gibalne količine molekul plina. Parameter, ki ta pojav opisuje, je efektivni akomodacijski koeficient gibalne količine (angl. effective tangential momentum accommodation coefficient, ETMAC), definiran kot relativna sprememba vzdolžne komponente hitrosti molekule po trku s površino. V tem delu je raziskan vpliv tega parametra v dveh aplikacijah: pri kalibraciji merilnikov z lebdečo kroglico (angl. spinning rotor gauge, SRG) ter pri prevodnosti cevi.

SRG je tlačni merilnik, ki deluje na principu molekulskega upora. Molekule plina, ki obdajajo vrtečo se kovinsko kroglico, neprestano trkajo z njeno površino, ter ji s tem odvzemajo vrtilno količino. Posledično zaviranje kroglice je neposredno povezano s tlakom plina, ki obdaja kroglico. ETMAC v takem merilniku igra vlogo kalibracijske konstante, določitev katere je izjemno pomembna pri zmanjšanju merilne negotovosti merilnika.

Ker je vrednost ETMAC odvisna od plina, kalibracija SRG zajema določitev te vrednosti za vsak plin, za katerega bo merilnik uporabljen. Celoten postopek kalibracije je lahko tako precej časovno zahteven. Dodatno težavnost pa predstavljajo tudi mešanice plinov, ki so lahko v uporabi. V tem delu smo z raznimi površinskimi obdelavami kroglic želeli zmanjšati plinsko odvisnost ETMAC. Če bi lahko to odvisnost zmanjšali, bi bila za kalibracijo SRG potrebna le kalibracija z enim plinom, merilna negotovost pa bi kljub temu ostala nizka tudi za ostale pline. Ugotovili smo, da povečanje hrapavosti površine kroglice z jedkanjem v kislini opazno zmanjša plinsko odvisnost ETMAC za šest plinov: helij, metan, neon, dušik, argon ter kripton. Največji odmik od povprečne vrednosti ETMAC se je pokazal pri heliju in neonu, ki sta najlažja žlahtna plina. Če tadva plina izvzamemo iz izračunov, je plinska odvisnost za preostale pline na jedkani površini približno dvakrat manjša v primerjavi s polirano kroglico.

Plinska odvisnost je bila prav tako raziskana za primer prevodnosti dolge cevi, narejene iz nerjavečega jekla. V molekularnem režimu je številska gostota molekul plina dovolj nizka, da te med potovanjem skozi cev ne trkajo druga z drugo. Vsi trki so tako trki med molekulo in površino cevi.

V ta namen smo razvili merilno metodo za merjenje prevodnosti cevi, iz katere smo izračunali vrednost ETMAC. Za to metodo je potreben le en merilnik tlaka. Dodatna prednost te metode je v tem, da kalibracija merilnika ni potrebna, v kolikor ima ta merilnik linearen odziv. Merilna negotovost vrednosti ETMAC, dobljenih s to metodo, je bila manjša kot 0.5 %.

Za razliko od kroglic SRG, se plinska odvisnost na cevi močno zmanjša tudi za helij in neon. Plinska odvisnost hrapave cevi je približno petkrat manjša kot na polirani cevi.

Contents

List of Figures

List of Tables

Abbreviations

AFM ... atomic force microscope
CDG ... capacitive diaphragm gauge
DCR ... deceleration rate
EA ... European co-operation for Accreditation
ETMAC ... effective tangential momentum-accommodation coefficient
IMT ... Institute of Metals and Technology
IPS ... Jožef Stefan International Postgraduate School
SEM ... scanning electron microscope
SRG ... spinning-rotor gauge
TMAC ... tangential momentum-accommodation coefficient

Symbols

A ... tube cross-section
$\bar{c}$ ... mean thermal velocity of gas molecules
C ... conductance
d ... tube diameter
DCR ... deceleration rate
d_{m} ... gas-molecule diameter
f ... ratio of diffuse reflections
k_{B} ... Boltzmann constant
Kn ... Knudsen number
l ... tube length
n ... particle number density
p ... pressure
P ... transmission probability
q_N ... particle flow
q_{pV} ... flow rate
R ... expansion ratio
R_{a} ... arithmetic average roughness
RD ... residual drag
Re ... Reynolds number
S_{q} ... root-mean-square roughness
s_{t} ... standard uncertainty of measured time intervals between zero crossings of the SRG signal voltage
T ... temperature
u ... standard uncertainty of measurement
U ... expanded uncertainty of measurement
V ... volume
w ... relative standard uncertainty of measurement
W ... expanded relative uncertainty of measurement
α ... angle of microstructures
Δt ... SRG sampling interval
η ... gas viscosity
λ ... mean free path
ν ... frequency of the SRG rotor
ρ ... gas density
σ ... tangential momentum-accommodation coefficient (TMAC)
σ_{eff} ... effective tangential momentum-accommodation coefficient (ETMAC)

Chapter 1

Introduction

Gas-flow dynamics is an active field of research, a statement that is best supported by special journal issues in recent years [1]–[3]. The main goal of these special issues was to join the numerical modelling, mainly performed in the rarefied dynamics community, and the experimental results coming mainly from the vacuum community, on a wide range of subjects, such as vacuum science, vacuum metrology, microfluidics, particle physics, and nuclear physics.

A vast majority of the published articles on gas dynamics concern numerical solutions to gas-flow phenomena, whereas experimental research is scarce. Additionally, the numerical analysis of gas flow often neglects the real characteristics of real-world systems, such as variations in the nominal system dimensions or surface roughness. Precise as they may be, the numerical results can deviate by up to a few ten percent from the experimental data. This is why the work presented in this thesis takes an experimental approach. It encompasses measurements of gas-flow conductance in systems with varying surface conditions. Furthermore, since this work demands that the pressure measurements are made with a very low measurement uncertainty, attention is also given to the optimization of the working conditions of the pressure gauges that were used in the experiments.

1.1 Gas Flow

1.1.1 Conductance

When two reservoirs filled with gas at different pressures are connected, a gas flow is established from the reservoir with the higher pressure to the one at the lower pressure, as is schematically shown in Figure 1.1. The rate of change of pressure inside both reservoirs is limited by the element that connects them (e.g., tube, aperture). The quantity that dictates this rate of change is called the conductance. In thermal equilibrium, when $T_1 = T_2$, conductance is defined as [4]

$$C = \frac{q_{pV}}{p_1 - p_2}; \quad q_{pV} = \frac{\mathrm{d}\,(pV)}{\mathrm{d}t}. \tag{1.1}$$

Here, q_{pV} is the *throughput* and it stands for the rate of change of the product of pressure and volume. Under the conditions indicated in Figure 1.1 the gas flows into volume V_2. If V_2 is constant for the whole duration, the throughput is simply the volume multiplied by the rate of change of the pressure, $q_{pV} = V_2 \dot{p}_2$.

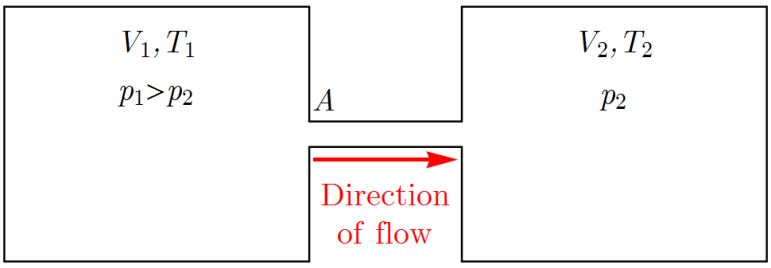

Figure 1.1: A schematic of gas flow. Two reservoirs with volume V_1 and V_2 containing gas at different pressures p_1 and p_2 and temperatures T_1 and T_2 are connected with a tube with a cross-section A. Gas flow is established from the reservoir with the higher pressure to the one with the lower pressure.

1.1.2 Flow Regime

Gas molecules are discrete particles whose behaviour, at high number densities, becomes challenging to predict due to the interactions between them. This is why gas at higher pressures has been historically treated as a viscous medium similar to a liquid. On the other hand, interactions between the molecules are rare in the case of very low pressures, which means that they behave independently of each other. It therefore comes as no surprise that gas flow must be treated differently, depending on the flow regime. The parameter that distinguishes between the different regimes is called the Knudsen number [4]. It is defined as

$$Kn = \frac{\lambda}{d}; \quad \lambda = \frac{3}{4\pi n {d_\mathrm{m}}^2}, \tag{1.2}$$

where λ is the mean free path of the molecules, n is the number density of gas molecules, d_m is the molecular diameter, and d is the characteristic dimension of a gas-flow element (e.g., the diameter of the tube in Figure 1.1).

The ideal-gas law describes the relationship between pressure and number density as [4]

$$p = nk_\mathrm{B}T. \tag{1.3}$$

Here, p is the pressure, k_B is the Boltzmann constant, and T is the gas temperature. From Equations (1.2) and (1.3) it is clear that the Knudsen number Kn and pressure p are inversely proportional. A large value of the Knudsen number therefore corresponds to low pressures, and vice versa. Equation (1.2) states that Kn is the ratio between the mean free path of the gas molecules and the characteristic dimension of the system. At high values of Kn, λ is much larger than d, which means that the molecules collide mostly with the surface of the vacuum system. The molecules therefore traverse the chamber mostly unimpeded between collisions with the chamber's surface. This regime is called the *molecular flow* regime. On the other hand, molecules at a low value of Kn collide mostly with other molecules. This leads to a viscous behaviour of the gas at high pressures, called the *viscous flow* regime.

Since the two distinct flow regimes lie at both extremes of the value Kn, the border between them is loosely defined. In practice, the ideal molecular flow regime is hard to achieve, and gas flow is usually a combination of both regimes. This is called the *transitional flow* regime, which corresponds to the range of Kn values where the flow is neither molecular nor viscous. An agreed-upon interval for the transitional flow regime is $0.01 < Kn < 0.5$ [4], where viscous flow occurs at $Kn < 0.01$ and the molecular at $Kn > 0.5$. A schematic of the two flow regimes at extreme values of Kn is shown

in Figure 1.2 for the case of flow through a tube. A path that a single molecule takes after entering the tube, as shown in Figure 1.2 on the left-hand side, is characteristic for molecular flow. For the viscous flow regime (right-hand side) streamlines are used to demonstrate the flow of a viscous gas.

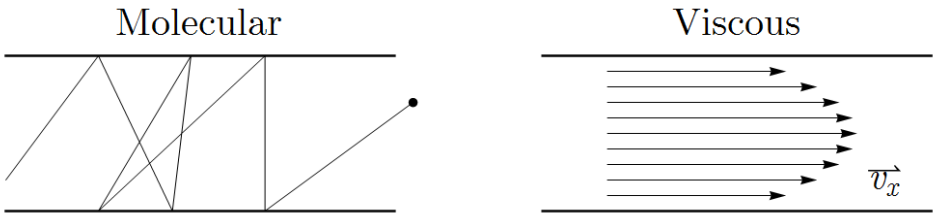

Figure 1.2: A schematic of two flow regimes. At very low pressures, molecules travel through the tube independently of each other and change directions only after colliding with a surface (left). At high pressures, collisions between molecules are much more frequent, and the gas behaves like a viscous medium (right). Molecular flow is represented with a molecule's trajectory and viscous flow with streamlines.

In the following text, the viscous and the molecular flow regimes are described in more details, where the focus is on the flow through a straight tube with a circular cross-section.

1.1.2.1 Viscous Flow

At high pressures (corresponding to low Kn) the collisions between gas molecules are much more frequent than those between a molecule and the surface of the vacuum chamber, which makes tracking the movement of each molecule impossible. That is why gas in this regime can be more easily be considered as a continuous medium. However, the geometry and conditions of real-world vacuum systems are not ideal. This can include curved tubes and tubes whose cross-section changes along its length. Additionally, the surface conditions of the tube greatly affect its conductance [5]–[7]. These complications render an analytical approach to accurately determine conductance impractical, and a numerical approach must be taken.

The difficulty of obtaining a numerical solution relies heavily on the nature of the viscous flow, determined with the *Reynolds number* [4]

$$Re = \frac{\rho v d}{\eta}. \tag{1.4}$$

Here, ρ is the gas density, v is the flow velocity, and d is the diameter of the tube. For low values of Re the flow is laminar, and the streamlines are linear (as seen in Figure 1.2). On the other hand, for high values of Re, viscous flow can become turbulent. Here, streamlines are unstable and vortices are introduced to the flow, resulting in a lower overall conductance [4]. Since the flow velocity v is hard to determine experimentally for gas flow, it can be rewritten as

$$v = \frac{1}{A}\frac{\mathrm{d}V}{\mathrm{d}t} = \frac{4}{\pi d^2}\frac{q_{pV}}{p}, \tag{1.5}$$

which results in Re having the form

$$Re = \frac{32}{\pi^2}\frac{q_{pV}}{\eta \bar{c}^2 d}; \quad \bar{c} = \sqrt{\frac{8 k_\mathrm{B} T}{\pi m}}. \tag{1.6}$$

In the last step, the ideal-gas law from Equation (1.3) was used and the mean gas velocity $\bar{c}$ was introduced. Similar to the molecular and viscous flow regimes, the transition from

laminar to turbulent flow is not well defined, but in practice approximate values are chosen. For the case of gas flow through a circular tube, the limits are [4]

$$Re \begin{cases} < 2300 & \text{for laminar flow} \\ > 4000 & \text{for turbulent flow} \end{cases} \tag{1.7}$$

The throughput for the case of laminar flow through a straight cylindrical tube is [4]

$$q_{pV} = \frac{\pi}{256}\frac{1}{\eta}\frac{d^4}{l}\left(p_1^2 - p_2^2\right), \tag{1.8}$$

where l is the length of the tube. Therefore, the conductance

$$C = \frac{\pi}{256}\frac{1}{\eta}\frac{d^4}{l}\left(p_1 + p_2\right) = \frac{\pi}{128}\frac{1}{\eta}\frac{d^4}{l}\bar{p}; \quad \bar{p} = \frac{p_1 + p_2}{2} \tag{1.9}$$

is proportional to the mean pressure inside the tube $\bar{p}$.

1.1.2.2 Molecular Flow

At very high values of Kn the gas molecules travel through the tube unimpeded by other molecules, due to their very low number density, and most collisions occur between a molecule and the tube's surface.

The parameter that determines the conductance of a tube is called the *transmission probability*, defined as the ratio between the particle flow exiting the tube q_{N2} and the particle flow entering it q_{N1}, where the particle flow is defined as the number of particles crossing the entrance in a unit of time. The transmission probability P is then defined by [4]

$$q_{N2} = q_{N1}P. \tag{1.10}$$

The incoming particle flow rate q_{N1} into the tube with a cross-section area A equals [4]

$$q_{N1} = \frac{1}{4}n_1\bar{c}_1A. \tag{1.11}$$

This result is taken from the kinetic theory of gases where molecules are modelled as hard spheres. q_{N1} is equivalent to the number of molecules striking an area A per unit time. Since some particles also enter the tube through the other end, the net particle flow q_{N} through the tube is

$$q_N = \frac{\bar{c}}{4}AP\left(n_1 - n_2\right). \tag{1.12}$$

Since the particle flow and the throughput are related $q_{\mathrm{N}}/n = q_{\mathrm{pV}}/p$ [4], the conductance is then

$$C = \frac{\bar{c}}{4}AP. \tag{1.13}$$

In the case of an aperture (infinitely short tube) the equation is easy to solve, since no molecule can collide with the aperture's (infinitely thin) surface. The transmission probability therefore equals $P = 1$, and the conductance equals $C = \bar{c}A/4$.

For longer tubes, the molecules collide with the tube's surface several times. The analytical calculation of the transmission probability is therefore not that straightforward, and numerical methods are normally used. Still, analytical approximations exist for a circular tube of arbitrary length l and diameter d [4]

$$C = \frac{\pi}{16}\bar{c}d^2\frac{14 + 4\frac{l}{d}}{14 + 18\frac{l}{d} + 3\left(\frac{l}{d}\right)^2}. \tag{1.14}$$

In the limit of small l the above equation becomes the same as for an aperture with a cross-section $A = \pi d^2/4$. Conductance over a wider range of l is shown in Figure 1.3.

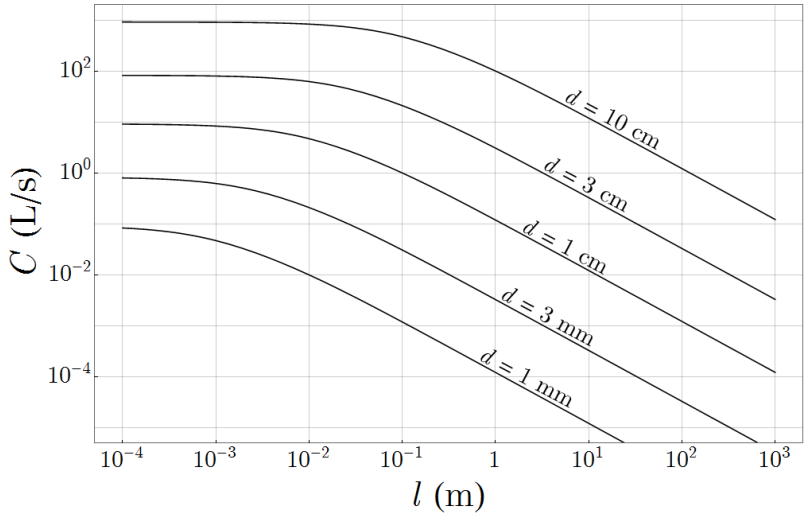

Figure 1.3: Conductance of a circular tube as a function of its length is calculated for several values of diameter d, using Equation (1.14).

1.1.2.3 Transitional Flow

Between the viscous and the molecular flow regimes, $0.01 < Kn < 0.5$, neither Equation (1.9) nor Equation (1.14) applies, and another approach must be taken. The tube can be treated as a pair of parallel tubes, where one has molecular, and the other viscous conductance [4]. In this case $C \approx C_{\text{molecular}} + C_{\text{viscous}}$, and an analytical solution can then be written as [4]

$$C = \frac{\pi}{12}\left(\frac{3}{32}\cdot\frac{\bar{p}d}{\eta\bar{c}} + Z\right)\frac{d^3}{l}\bar{c}. \tag{1.15}$$

Here, the dimensionless parameter Z is introduced to characterize the behaviour in the transitional flow regime. A semi-empirical expression for Z in the case $p_1 \approx p_2$ was developed by Knudsen [8] in the form

$$Z = \frac{1+\sqrt{\frac{8}{\pi}\frac{\bar{p}d}{\eta\bar{c}}}}{1+\frac{21}{17}\sqrt{\frac{8}{\pi}\frac{\bar{p}d}{\eta\bar{c}}}}. \tag{1.16}$$

The parameter Z was introduced in order to better describe phenomena in the transitional regime, which could not be described by assuming $Z = 1$. Conductance over a wide range of Kn is shown in Figure 1.4 (solid line), as calculated from Equation (1.15) for the case of the flow of nitrogen at room temperature through a circular tube of length $l = 1$ m and diameter $d = 1$ cm.

The most notable phenomenon in the transitional regime is the emergence of the Knudsen minimum, as seen in Figure 1.4. Experiments have repeatedly shown the appearance of the minimum in the conductance near $Kn \approx 1$, however the exact position of the minimum can vary with the geometry of the system [8]–[12]. This minimum is most pronounced in longer tubes [8] and is attributed to two competing phenomena: self-diffusion and drift [13]. Self-diffusion of gas molecules occurs at $Kn \gg 1$, where a fraction of molecules travel parallel to the tube's surface. Due to their long free path they can traverse the whole length of the tube unimpeded, leading to an increase in conductance. Drift, on the other hand, occurs at $Kn \ll 1$. Here, the collisions between molecules are so frequent they start to drag each other along their path. This again leads to an increase in conductance. At $Kn \approx 1$,

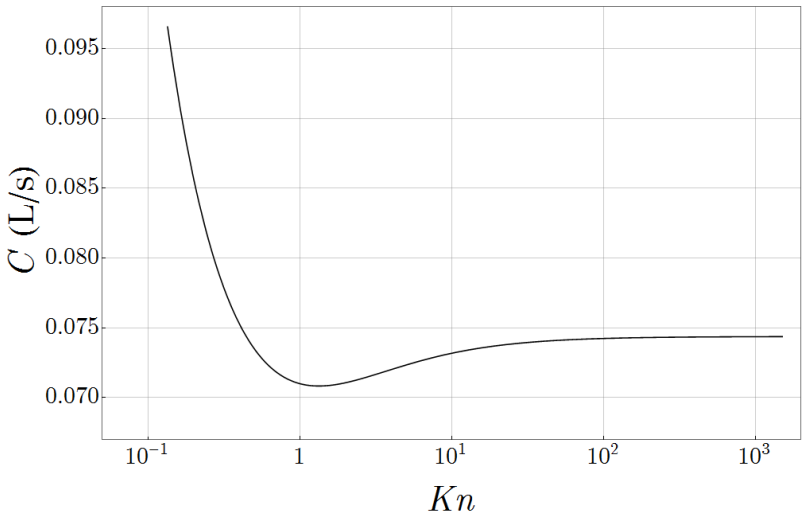

Figure 1.4: Conductance of a circular tube of length $l = 1$ m and diameter $d = 1$ cm over a wide range of Kn, calculated from Equation (1.15) for the case of nitrogen flow at room temperature.

however, molecules travelling parallel to the tube's surface change course due to occasional collisions with other molecules, and cannot traverse the tube's length in a straight line. This, coupled with the fact, that drift is weak in this regime, leads to an overall decrease in conductance. This model is well supported with experimental data [14].

1.2 Momentum Accommodation

Consider a molecule striking a flat surface. In the simplest case the molecule is instantly reflected with the tangential component of its velocity unchanged. This is called the *specular reflection*, and it happens when the molecule does not interact with the surface. If the molecule does interact with the surface, it can be temporarily adsorbed onto the surface after the collision. The molecule then leaves the surface after a short adsorption time, but due to momentum accommodation, its trajectory follows a cosine distribution probability. This type of reflection is called the *diffuse reflection*. Maxwell introduced a model [15] in which he defined a parameter f to describe the nature of reflections. He proposed that out of all the molecules that collide with a specific surface, a fraction f is reflected diffusely, and $(1-f)$ that are reflected specularly. In practice, however, a parameter called the tangential momentum accommodation coefficient TMAC is used, which signifies the average change of a molecule's tangential component of velocity after the collision. The TMAC therefore equals 1 for diffuse and 0 for specular reflections.

In practice, surfaces are never ideally flat and some roughness is always present. In this case, even though a single molecule might be reflected specularly, molecules on average appear to scatter diffusely, due to each molecule striking a differently angled facet, depending on the structure of the surface. This is why in practice the effective tangential momentum-accommodation coefficient, ETMAC, is introduced, which encompasses the collective behaviour of all the molecules in a gas flow.

Experimental investigations show that the ETMAC in practice is usually around 1, although often its value can be larger than that. By its definition, it appears that a fraction of molecules are reflected backwards, in what is called *backscattering*. Although unintuitive, this phenomenon is supported in the literature [5], [9], [16]–[18] and occurs on

macroscopically rough surfaces.

The specular and diffuse reflections, and backscattering are schematically shown in Figure 1.5. For each, expected values of the ETMAC σ_{eff} are given, along with the average tangential components of the molecule's velocity before $\overline{v_0}$ and after $\overline{v_1}$ collision. Also shown are the angular distributions for diffuse reflection and backscattering.

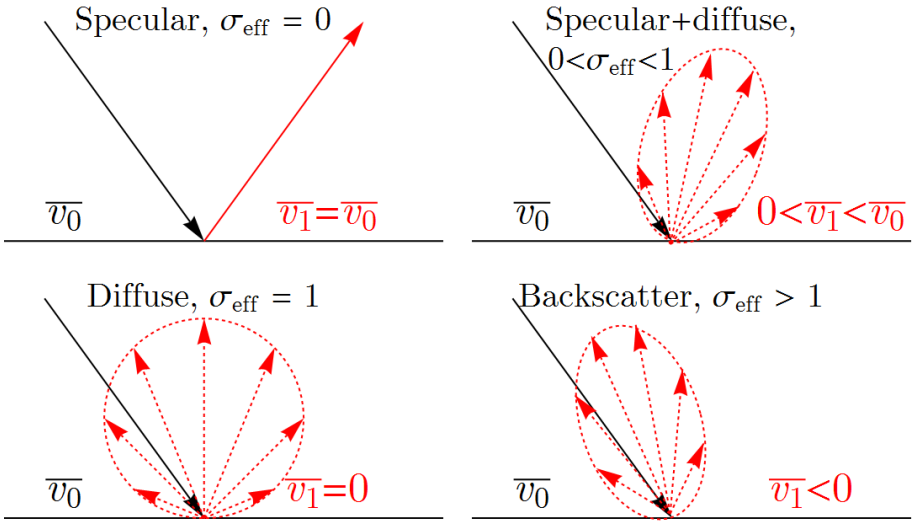

Figure 1.5: Different reflection scenarios are shown for different values of the ETMAC: specular reflection, a combination of the specular and diffuse reflection, diffuse reflection, and backscattering. Expected values of the ETMAC σ_{eff} are also given, along with the angular distribution of reflected molecules.

A value of ETMAC different than unity can therefore affect the conductance of an element, through which gas flows (e.g., a tube). The conductance in the molecular flow regime is proportional to the correction factor [19]

$$C \propto \frac{2-\sigma_{\text{eff}}}{\sigma_{\text{eff}}}. \tag{1.17}$$

In the viscous-flow regime this dependence takes a more complicated form and is beyond the scope of this thesis. Therefore, if the surface is altered, the changes in conductances can be drastic [7], as will be shown in Chapter 5.

The ETMAC is in practice never close to zero, even for atomically clean surfaces. For instance, the measured σ_{eff} values on silver and titanium surfaces, obtained by in-situ evaporation on a very flat glass surface, were not smaller than 0.71 for helium, and were between 0.80 and 0.92 for neon, argon, and krypton [6]. In practical applications in vacuum systems, technical surfaces, such as stainless steel, aluminium, and copper, may appear to be flat. However, adsorbate and oxide layers which are present even in ultra-high vacuum conditions, lead to almost completely diffuse molecule scattering, and the ETMAC is close to 1. The topology of the surface is of extreme importance to the value of the ETMAC. Both experimental and numerical studies regarding the effect of surface geometry show that both the height and inclination of surface features strongly affect the ETMAC [5], [20].

While many approaches have been made in the past to determine the ETMAC [9], [21], this area of research gained new popularity with the invention of the spinning rotor gauge (presented in Section 1.3) in the latter half of the previous century. Due to the gauge's

direct reliance on the ETMAC, the necessity of accurately determining its value became of great importance. Typical ETMAC values reported in the literature for steel rotors with a polished surface measured with nitrogen lie in the range $0.94 < \sigma_{\text{eff}} < 1.06$ [22], and for rotors with a roughened surface (sandblasted, etched) values up to $\sigma_{\text{eff}} = 1.2$ [22], [23] were measured. Surface roughness therefore greatly affects the ETMAC. In addition to this, dependence of the ETMAC on gas species has been reported in numerous studies, where this dependence results in a difference of a few percent for polished surfaces [23]–[26]. On roughened surfaces this difference is reported larger, and the ETMAC for lighter gases, such as helium and neon, are reported to be further from 1 than for heavier gases [23]. The ETMAC is therefore more sensitive to changes in the surface conditions for lighter gases than for heavier gases.

1.3 Spinning Rotor Gauge

When a gas molecule collides with a surface, their tangential momentum changes, if $\sigma > 0$ (by definition). Therefore, if the surface is moving in the tangential direction, the colliding molecules act as a decelerating force, called the *molecular drag*. Because the number of molecules that collide with a surface in an arbitrary time frame is proportional to the number density of gas molecules, and because an average force from a single collision can be determined as well, the gas pressure can be directly determined from observing the drag force acting on a surface moving through the gas.

The spinning rotor gauge utilizes this phenomenon to measure the pressure inside vacuum chambers. Here, pressure is calculated from the rate of deceleration of a rotating steel ball bearing (rotor), which is rotating freely at a few hundred Hz. A schematic of the gauge's components is shown in Figure 1.6.

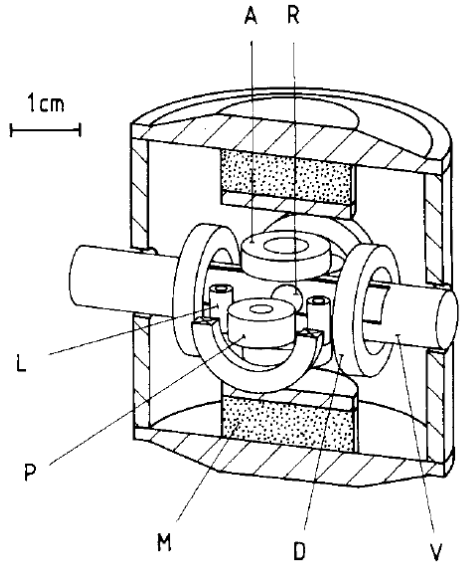

Figure 1.6: Schematic of a spinning rotor gauge [27]: R - rotor; V - thimble connected to the vacuum system; M - permanent magnet; A - coil for control of axial rotor position; L - lateral damping coil; D - drive coil; P - pickup coil.

The rotor is situated inside a thimble, which is closed at one end and connected to the vacuum chamber at the other end. The measuring head slides on the thimble and

envelops the rotor. In order to remove deceleration due to mechanical friction of the rotor against the surface of the thimble, the rotor is magnetically levitated with a combination of permanent magnets and position stabilization coils (vertical and lateral), which are situated in the measuring head. In order to achieve levitation, the rotors must be of a diamagnetic metal, usually a chrome steel. The rotation of the rotor can be activated by a rotating magnetic field produced by driving coils positioned around the thimble.

A pair of pickup coils is used to measure the rotation frequency of the rotor. When suspended in the magnetic field the rotor tends to orient itself so that its magnetic moment is aligned with the external magnetic field. However, real rotors are never completely spherical, and the axis of the rotor's rotation tends to align with its largest principal moment of inertia [28]. This leads to the fact that the magnetic moment of the spinning rotor is not perfectly aligned with the external magnetic field, and can be broken into a static component (aligned with the magnetic field) and a rotating component. This rotating component is crucial to the operation of the SRG, as it induces an AC voltage signal in the pickup coils [27].

The measuring process is this. First, the driving coils accelerate the rotor to the desired operational frequency. Usually, this is about 400 Hz. The driving coils are then switched off until the rotor's frequency falls below a set threshold. This frequency window is usually 10 Hz to 20 Hz wide. The rotor's frequency decays due to molecules' collisions with its surface in a set time frame (sampling interval), by measuring the increase of the time interval between successive crossings of induced AC pickup signal through a 0 V level. In order to reduce the scatter of readings, a multi-period algorithm is used [29]. The pressure around the rotor is calculated from the deceleration rate DCR as [28] the

$$p = \sqrt{\frac{8k_{\mathrm{B}}T}{\pi m}}\frac{\pi\rho r}{10\sigma_{\mathrm{eff}}}DCR - RD; \quad DCR = \left(-\frac{\dot{\nu}}{\nu}\right) \tag{1.18}$$

where r and ρ are the rotor's radius and density, respectively, and ν is the rotor frequency. σ_{eff} is the effective tangential momentum-accommodation coefficient, ETMAC, defined in Section 1.2.

Finally, RD in Equation (1.18) is the residual drag. The residual drag is the zero reading of the SRG at zero pressures, which occurs due to the pressure-independent deceleration of the rotor, a consequence of effects such as temperature-induced changes in the rotor's moment of inertia, electromagnetic interactions between the rotor and the suspension circuitry, and eddy currents [28], [30], [31]. The eddy currents are induced in both the rotor and the metal thimble surrounding it, due to the spinning magnetic moment of the rotor [28], [31]. The deceleration due to eddy currents induced in the thimble can be greatly reduced by using a glass thimble [32], but these can be harder to make and are prone to breaking. Therefore, steel thimbles are mainly used.

The temperature of the rotor has a large effect on the stability of the SRG, due to its thermal expansion. When the rotor heats up (or cools down), it expands (shrinks). Due to the conservation of angular momentum this causes the rotor to decelerate (accelerate), which affects the residual drag. In the presence of temperature drifts around the SRG, an additional term must be added to Equation (1.18), so that [4]

$$p = \sqrt{\frac{8k_{\mathrm{B}}T}{\pi m}}\frac{r\rho\pi}{10\sigma_{\mathrm{eff}}}\left(DCR - 2\alpha\frac{\mathrm{d}T_{\mathrm{rotor}}}{\mathrm{d}t}\right) - RD. \tag{1.19}$$

Here, α is the coefficient of thermal expansion of the rotor material, and T_{rotor} is the rotor temperature. Because of the position of the rotor during operation its temperature cannot be measured directly, which is why determining the second term in Equation (1.19) is difficult. Even though models to determine the rotor temperature from the temperature

measured directly on the thimble have been proposed in the past [33], it is nevertheless recommended that the temperature inside the room where the SRG is operated is kept constant, and the SRG is thermally insulated. In addition to changes in the temperature inside the room, the rotor and the measuring head are heated during each re-acceleration of the rotor, due to electrical resistance heating of the driving coils and eddy currents in the thimble and rotor. At higher pressures, above 1 Pa, rotor re-accelerations occur much more frequently and the change in rotor temperature is much more significant. Additionally, prior to operating the SRG the rotor must be driven to the desired frequency from rest. This significantly heats up the rotor and the surrounding thimble [30]. Due to slow thermalization of the rotor at low pressures (the rotor can exchange heat with the surrounding thimble only by radiation), it is standard practice that the SRG rests for at least 6 hours after initial acceleration before it is used for pressure measurements [4].

In deriving Equation (1.18) the assumption of a molecular flow regime was made, so the equation is valid only when $\lambda > d$. Here, d refers to the distance between the rotor and the thimble, which is of the order of a few mm. This sets the practical upper operational limit to about 1 Pa, where deviation from a linear response in the molecular regime is less than 2 % [4], [34]. At pressures higher than that, the interactions between gas molecules inevitably lead to the creation of a rotating layer of gas surrounding the rotor. This rotating layer reduces the molecular drag on the rotor and with it the sensitivity of the SRG. Furthermore, due to the non-spherical symmetry of the gauge's assembly (sphere inside a cylindrical thimble), turbulence can occur. While these complications can be overcome by taking into account the geometry of the assembly, the temperature compensation, and the gas-viscosity corrections [35], [36], the uncertainty of pressure measurements increases significantly, which usually leads researchers to use other pressure gauges, optimized for operating in higher pressure ranges.

Due to its excellent long-term stability and its linear response, the SRG has been used in this work as the main pressure gauge for determining the changes of the ETMAC of a long tube after various surface treatments in Chapter 5. Additionally, due to its reliance on the ETMAC of its rotor (Equation (1.18)), it has been used in a study of the influence of surface conditions on the changes of the ETMAC of its rotor in Chapter 6.

Chapter 2

Aims and Hypotheses

This thesis encompasses the study of the influence of surface conditions on momentum accommodation. In pursuit of this, two approaches were taken: one was changing the surface of a long stainless-steel tube and observing its conductance, and the other was changing the surface of the rotors of the SRG and directly measuring the ETMAC. Since the SRG played a vital role in both approaches, its measurement capabilities had to have been determined prior to this work. One part of this thesis is therefore dedicated to pressure uncertainty as well.

2.1 Specific Aims

- Study of the effects of the working conditions of the SRG on the precision of zero correction, pressure measurements at the bottom of its measuring range, and optimization of the working conditions in order to minimize the measurement uncertainty of the SRG in the molecular flow regime at pressures below 10^{-4} Pa. The SRG will be the main gauge which will allow the target measurement uncertainty in gas-flow measurements in the molecular flow regime.
- Development of a new method for determining the flow conductance of a tube with a measurement uncertainty below 0.5 % in the molecular-flow regime with the possibility to extend to the transitional and the viscous flow regimes.
- Study of the influence of the tube's surface condition on the conductance in the molecular-flow regime and estimation of the change of the ETMAC.
- Study of the effects of different treatments, such as venting to the atmosphere, vacuum baking, and oxidation, which can affect the surface conditions of the SRG rotor and can cause changes in the calibration constants for different gases.

2.2 Hypotheses

Two main contributions dictate the SRG measurement uncertainty. The first is the ETMAC uncertainty for a specific gas, which depends on the measurement uncertainty of the calibration system and the stability of the ETMAC after calibration. The second contribution comes from the measurement accuracy of the relative deceleration rate of the rotor, which is expressed as the width of statistical distribution (scatter) of readings.

Hypothesis 1: *By optimizing the working conditions of the SRG, such as the sampling interval, rotor frequency, and the amplitude of the induced signal, we can minimize the scatter of the gauge's readings and therefore the measurement uncertainty.*

The measurement uncertainties of methods used for determining flow conductance, reported in literature, are above 1 %. This is unacceptable for the purposes of detecting small changes of the ETMAC due to changes in a tube's surface condition.

Hypothesis 2: *The SRG, which is a linear gauge with a high precision in the pressure range between* 10^{-5} Pa *and* 1 Pa*, can be used to construct a system to measure gas flow conductance with the measurement uncertainty <0.5 %. The ETMAC can be calculated from the measured conductance of a tube of well-defined dimensions, using an existing theoretical calculation derived by assuming ETMAC = 1.*

The ETMAC is a function of both the angle of the gas molecules, reflected from a surface, as well as the nature of the gas-surface interactions. The value of TMAC therefore depends not only on the surface morphology, but on the gas species used in the system as well. The SRG therefore requires calibration for each gas individually. Another complication arises in systems where gas mixtures are used and the ETMAC depends on the relative concentrations of the component gases.

Hypothesis 3: *The changes in the ETMAC of the SRG rotor and the tube should show similar behaviour (identical results are not expected, since the materials are different). Among the proposed treatments, we can be chosen to show the smallest variations of the ETMAC between gases. Calibration using only one gas will then be sufficient for a rotor treated in this way, if the ETMAC variation between the gases is lower than the required measurement uncertainty. Such surface treatments would then be recommended in applications where gas mixtures are used.*

Chapter 3

Methods

This chapter is divided into three sections. In Section 3.1, the work done on investigating the influence of the working parameters of the spinning rotor gauge on the measurement uncertainty is reported. In Section 3.2, the method with which the ETMAC of the SRG rotors was determined is presented along with the uncertainty of the result. Lastly, in Section 3.3, the method with which the conductance of a long stainless-steel tube (and from it the ETMAC) is presented in detail.

In the following chapters the measurement uncertainty is evaluated according to guidelines set by the European co-operation for Accreditation (EA) [37]. The terminology follows those guidelines as well. Unless stated otherwise, uncertainty is given as "standard uncertainty" with a coverage factor $k = 1$, which corresponds to a coverage probability of approximately 68 %.

3.1 Origins of SRG Uncertainty

The mathematical model of the pressure measurement with SRG is given in Section 1.3 by Equation (1.19). From this a measurement uncertainty of the SRG can be expressed as [38]

$$\frac{u(p_{\mathrm{SRG}})}{p_{\mathrm{SRG}}} = \sqrt{\left(\frac{u\left(\sigma_{\mathrm{eff}}\right)}{\sigma_{\mathrm{eff}}}\right)^2 + \left(\frac{u\left(LTS\right)}{LTS}\right)^2 + \frac{1}{4}\left(\frac{u\left(T\right)}{T}\right)^2 + \left(\frac{u\left(RD\right)}{p_{\mathrm{SRG}}}\right)^2 + \left(\frac{u\left(DCR\right)}{DCR}\right)^2}. \tag{3.1}$$

In the estimate we have neglected the uncertainty contribution due to the molecular mass of the gas, which is justified in a case when we measure a known pure gas. In addition, we have no uncertainty contributions due to the rotor radius and density when we use the same values of these parameters as during the calibration of σ_{eff} of the rotor. The standard uncertainty of the ETMAC $u\left(\sigma_{\mathrm{eff}}\right)$ is discussed in Section 3.2. $u\left(LTS\right)$ is the standard uncertainty due to the changes of the ETMAC after calibration. As was discussed in Section 1.2, the value of the ETMAC can change between calibrations due to changes of the rotor's surface. The value of $u\left(LTS\right)$ can be estimated from repeated periodic calibrations. $u\left(T\right)$ is the standard uncertainty of the gas temperature, which is estimated from the uncertainty of the thermometers used for the measurement of the temperature of the vacuum-chamber walls and variations of the temperature across the chamber. $u\left(DCR\right)$ is the standard uncertainty of the deceleration rate, respectively, which is expressed as the standard deviation of consecutive readings during pressure measurements. Finally, $u\left(RD\right)$ is the standard uncertainty of the residual drag and is determined prior to pressure measurements, when RD is determined at the base pressure.

The uncertainty of the temperature of the rotor T_{rotor}, defined in Equation (1.19), contributes to the pressure uncertainty as well. Because the temperature cannot be accurately measured during operation, its uncertainty is unknown and largely depends on several conditions (temperature of the gas, thimble and the measurement head). Since the rate of change of T_{rotor} directly affects the offset of the pressure measurement (see Equation (1.19) it can be combined with the residual drag. Thus, the term $u(RD)$ in Equation (3.1) encompasses not just the uncertainty of the residual drag, but of the rotor temperature as well.

3.1.1 Frequency Correction of the Residual Drag

The SRG operates in a pre-selected frequency window, usually 10–20 Hz wide. When operating at higher pressure, this frequency window can be larger in order to minimize frequent re-accelerations. An added complication to this, however, is that the residual drag is shown to be frequency-dependent, which leads to errors in the measured pressure. An example is shown in Figure 3.1. Here, the residual drag was measured in an evacuated vacuum chamber for two SRGs, here named SRG A (a) and SRG B (b), over a period of several days, while the frequency of both rotors was kept between 405 Hz and 425 Hz. It can

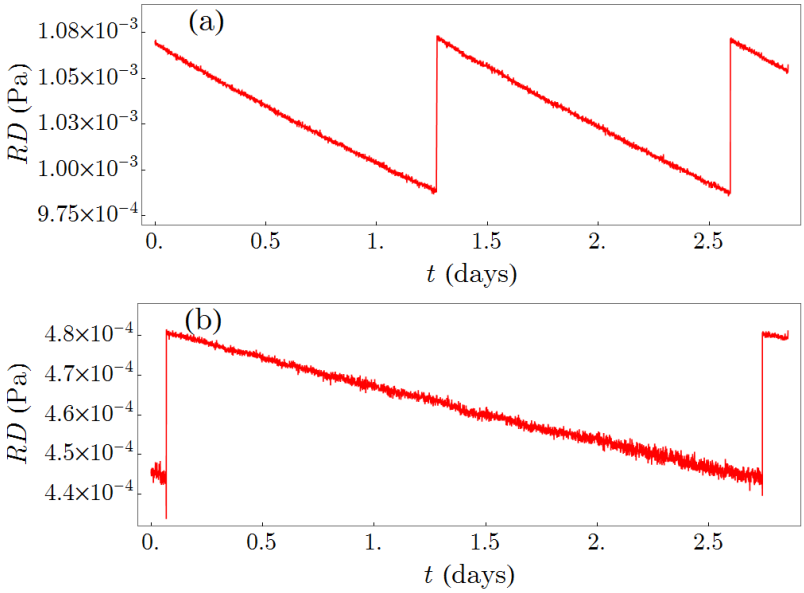

Figure 3.1: Residual drag measured over the course of several days for SRG A (a) and SRG B (b). The rotor frequency for both rotors was kept between 405 Hz and 425 Hz.

be seen that the residual drag for SRG A is roughly two times higher than for SRG B. This means that the rotor of SRG A must be re-accelerated more frequently. Additionally, the value of the residual drag changes in response to the changing rotor frequency. Therefore, if the frequency correction of the residual drag was not done for these rotors, an error of about 8×10^{-5} Pa for SRG A and 4×10^{-5} Pa for SRG B would be introduced to the pressure measurement. If, however, the rotor frequency is measured simultaneously with the pressure measurements, the frequency dependence of the residual drag can be directly determined. This is shown in Figure 3.2. Here, a linear fit $RD(\nu) = k \cdot \nu + RD_0$ was calculated using the least-squares method for SRG A (a) and SRG B (b). When the coefficients of the linear fit k and RD_0 are obtained, the pressure inside the chamber can be calculated by subtracting the linear fit from the pressure readings. The resulting corrected

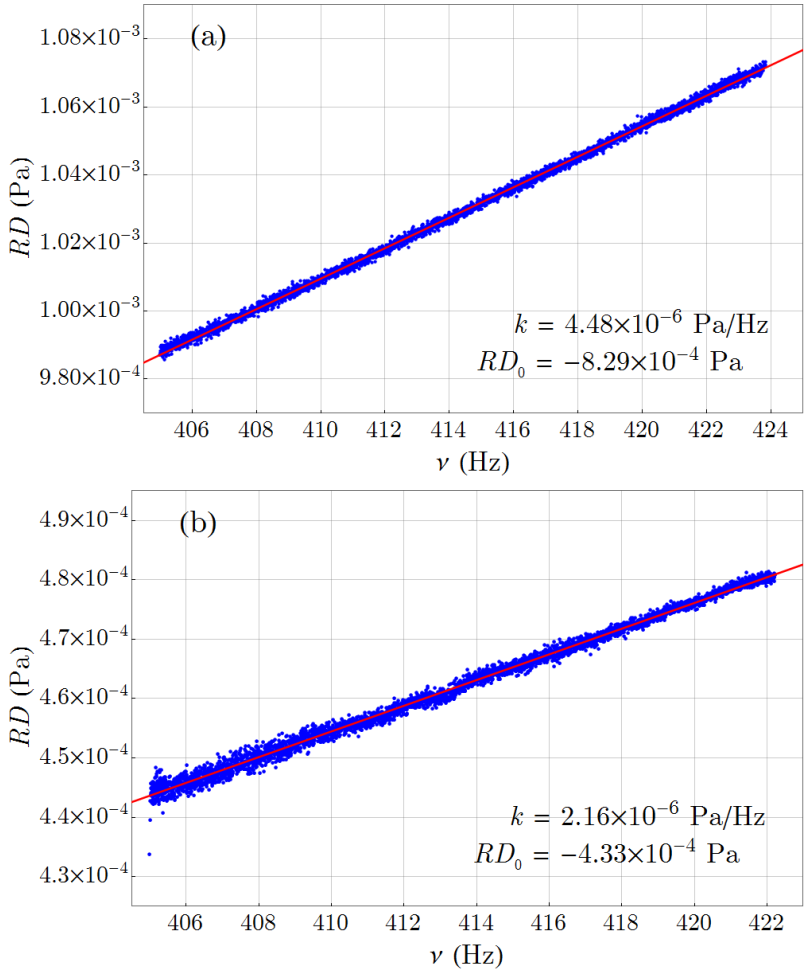

Figure 3.2: Residual drag as a function of the rotor frequency measured over the course of several days for SRG A (a) and SRG B (b). The linear fit is shown in red.

measured values at zero pressure are shown in Figure 3.3. By using this approach, the uncertainty contribution due to the residual drag was lowered by more than one order of magnitude to a level below 2×10^{-6} Pa.

In the previous example, a linear fit was used for the frequency correction of the residual drag. When operating at either a higher rotor frequency or a wider frequency window, a polynomial of a higher degree may be required, as can be seen in Figure 3.4. In addition to SRG A and SRG B from Figure 3.1, the residual drag was here measured for a third SRG, named SRG C, at several values of the rotor frequency between 400 Hz and 800 Hz. In this case, a quadratic fit was used for the frequency correction of the residual drag. The necessity for frequency corrections was especially important for SRG A and SRG B, while the residual drag for SRG 3 showed a minimal increase even at 800 Hz, compared to the other two.

3.1.2 Uncertainty of the Deceleration Rate

Several factors affect the standard uncertainty of the deceleration rate $u\,(DCR)$, defined in Equation (3.1), mainly the rotor frequency and the sampling interval [29]

$$u\,(DCR) = \frac{32 s_{\mathrm{t}}}{\sqrt{\nu}\,(\Delta t)^{5/2}}. \tag{3.2}$$

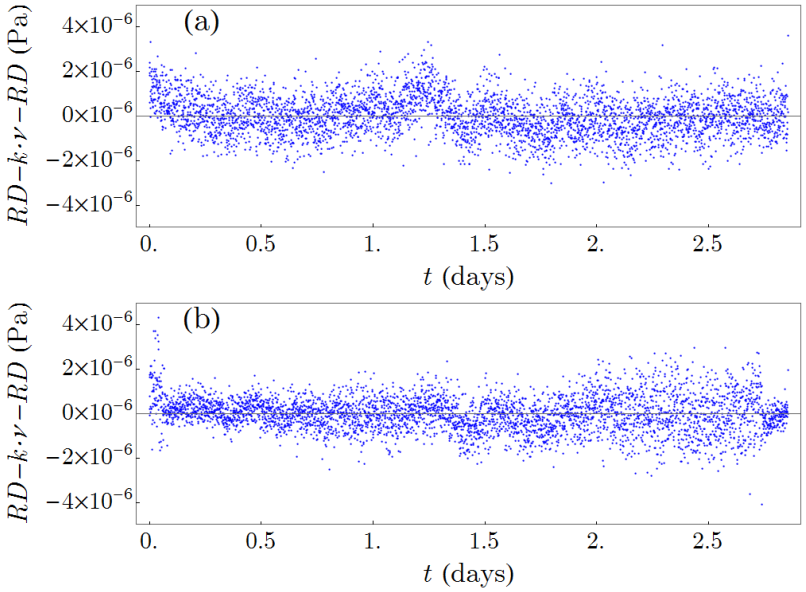

Figure 3.3: Residuals calculated by subtracting the linear fit in Figure 3.2 from measured residual drag in Figure 3.1 for SRG A (a) and SRG B (b).

Here, s_t is the standard uncertainty of the individual measured time intervals between zero crossings of the signal voltage measured in the pickup coils of the SRG and Δt is the sampling interval.

In addition to the frequency-dependent residual drag, the measurement precision (expressed as the standard deviation of repeated readings) of the SRG is expected to be inversely proportional to the square root of the rotor frequency, as per Equation (3.2). However, we discovered that the effect of the rotor frequency was stronger, where a twofold increase in the frequency led to a near tenfold decrease in the standard deviation. This study is presented in more detail in Chapter 4.

3.2 Calibration of the SRG

Some rotor-dependent variables, appearing in Equation (1.18), such as the radius r and density ρ are usually known to a high degree when the gauge is received from the manufacturer. These two values remain unchanged during the lifetime of the gauge. The only calibration constant therefore is the ETMAC σ_{eff}. Reported data show that the σ_{eff} of smooth steel rotor balls on average equals 1, with maximum deviation of (-4 % to +6 %) [26]. This means that the SRG can be considered as a primary pressure gauge with a standard uncertainty ($k = 1$) of 3 % using $\sigma_{\text{eff}} = 1$ for smooth rotors (polished surface). In practice, however, a lower uncertainty is often necessary and the rotor must therefore be calibrated. While σ_{eff} can be obtained from the initial calibration by the manufacturer, its value can change drastically during the rotor's lifetime [39]. Frequent calibration is therefore necessary in order to minimize the systematic error of the pressure measurements.

The ETMAC values, published in various journals, were obtained by leading national metrology institutes using primary standards with a state-of-the-art uncertainty for the generated pressure, of the order of 0.3 %. Often a nominal value of rotor diameter and density as given by the manufacturer is used instead of actual measured values. There may be an additional contribution to the uncertainty due to deviations from nominal values for

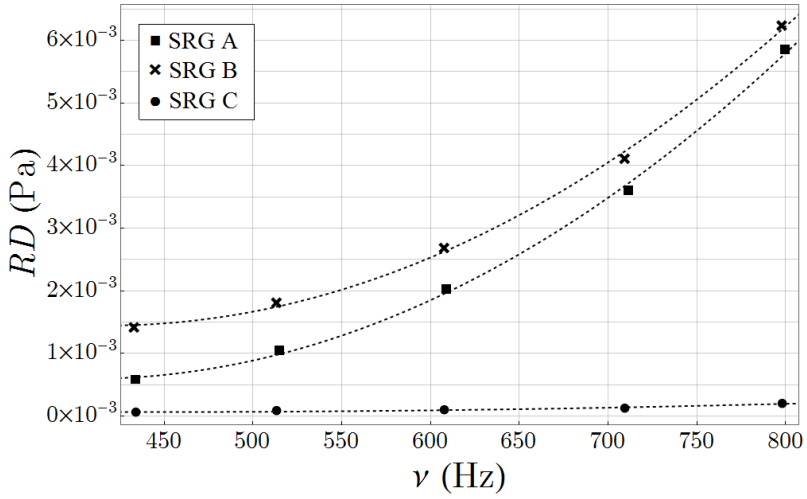

Figure 3.4: Residual drag as a function of the rotor frequency in the range from 400 Hz to 800 Hz. Here, a quadratic fit was used for frequency correction of the residual drag and is shown as a dashed line.

a rotor diameter of 0.2 % and the density of the rotor material of 0.5 %. A conservative estimate of the uncertainty for the ETMAC values for SRG rotors reported by national metrology institutes in the literature is therefore less than 1 %.

When calibrating the SRG with a reference gauge, first the SRG controller is set to $\sigma_{\text{eff}} = 1$. In this case the ratio of the SRG pressure to the reference pressure is equal to σ_{eff} of the rotor. Due to the viscosity effects at higher pressures, the ratio is linearly dependent on the reference pressure [40] for pressures below 2 Pa. σ_{eff} can therefore be determined by measuring the SRG-to-reference pressure ratio at several pressure points between 0.1 and 1 Pa [4], taking the extrapolated value of the ratio at zero pressure to be σ_{eff}. Its value is therefore obtained as the y-intercept of the calibration curve using the least-squares method. An example of the resulting calibration curve is shown in Figure 3.5, where p_{SRG} and p_{ref} are the SRG and the reference pressure, respectively. This calibration procedure was used for determining the ETMAC changes in Chapter 6.

For the purposes of determining σ_{eff} of a SRG rotor, it is crucial for the measurement uncertainty of the reference pressure to be as low as possible. The lowest possible uncertainty can be obtained with a primary method for the generation of a reference pressure. The use of a calibrated reference gauge already increases the uncertainty due to the time stability of its calibration factor after calibration.

For calibrations in the range from 10^{-2} Pa to 2 kPa, IMT has built a primary static expansion system. The equipment was purchased from European structural funds on the basis of the project "Infrastructure of the metrology system - Pressure" and is owned by the Republic of Slovenia. The system is still under metrological validation and some work presented in the present PhD is part of this validation. We have used the IMT static expansion system for the calibrations of SRG rotors presented in Chapter 6.

A simplified diagram of the primary static expansion method is shown in Figure 3.6. Here, gas is first introduced into the smaller chamber at pressure p_1. This initial pressure can be measured accurately using a reference gauge with a small measurement uncertainty, like a capacitance diaphragm gauge (CDG). The initial pressure can also be high enough to be traceable to an absolute pressure balance having a well-established traceability link to basic SI units.

The larger chamber is initially evacuated. When the valve connecting the two chambers,

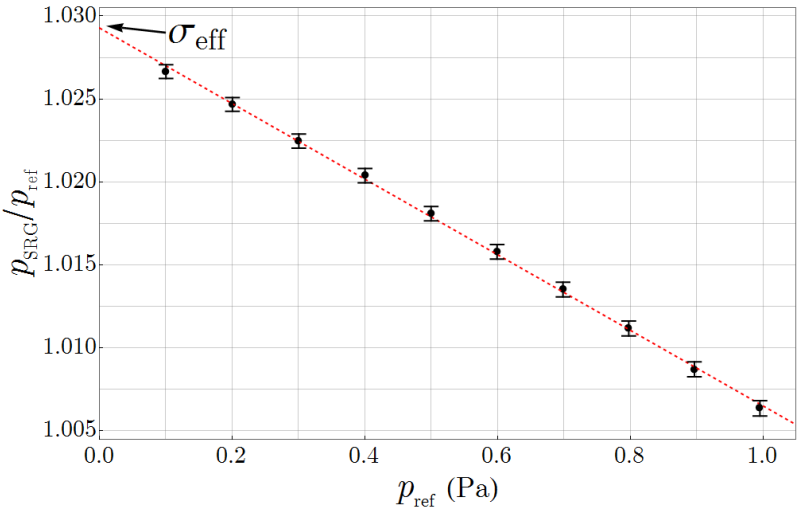

Figure 3.5: An example of an SRG calibration curve showing the linear dependence of the ratio of the SRG pressure p_{SRG} to the reference pressure p_{ref} on the reference pressure. The calibration constant σ_{eff} is determined as the y-intercept of the linear fit. Error bars represent standard uncertainty given in Figure 3.7.

Vlv-1, is opened, the pressures in both chambers equilibrate. This pressure, p_2, can be calculated by following the ideal-gas law

$$p_2 = \frac{p_1}{R}\frac{T_2}{T_1}; \quad R = \frac{V_1 + V_2}{V_1}. \tag{3.3}$$

Here, the expansion ratio R was introduced as the ratio of gas volumes before and after expansion. In a practical realization, the IMT system has two small chambers of approximately 5 ml and 0.25 L, and a large chamber of 37.01 L. For calibrations of the SRG we used expansions from the smallest initial chamber and the experimentally determined value of the expansion ratio was $R = 7.376 \times 10^3$.

After measuring p_2 with the SRG, both chambers should be evacuated and the process repeated at a higher initial pressure. This, however, would require a long pumping time, during which the temperature of the system might change, resulting in a higher uncertainty of the pressure measurement. In order to mitigate these complications, we use a method of accumulating the gas without evacuating the chambers between expansions. In this case the calculated pressure after the n-th expansion is

$$p_2^n = \frac{p_1^n}{R}\frac{T_2^n}{T_1^n} + \left(1 - \frac{1}{R}\right)\frac{T_2^n}{T_2^{n-1}}p_2^{n-1}, \tag{3.4}$$

where p_2^{n-1} was the calculated pressure in the chamber after the previous expansion.

3.2.1 Uncertainty of the SRG Calibration with the IMT Primary Static Expansion System

The measurement uncertainty of the ETMAC, obtained with the method described above, is determined by two contributions: the uncertainty of the ratio of the SRG pressure to the reference pressure, and the uncertainty deriving from linear regression. The relative uncertainty of the ratio can be obtained from

$$w\left(\frac{p_{\text{SRG}}}{p_{\text{ref}}}\right) = \sqrt{w\left(p_{\text{SRG}}\right)^2 + w\left(p_{\text{ref}}\right)^2}. \tag{3.5}$$

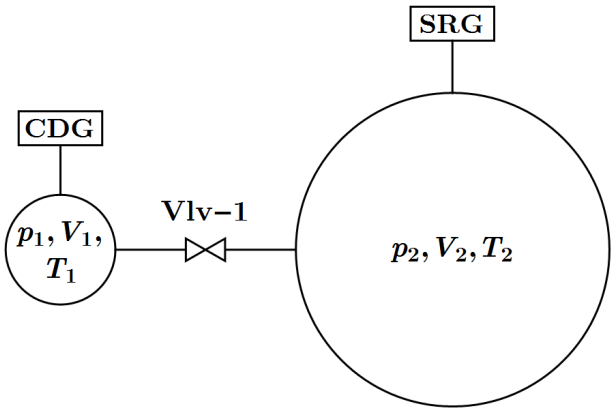

Figure 3.6: Schematic of the static expansion system. Gas at pressure p_1 is expanded from the left chamber. After opening the valve Vlv-1 gas occupies both chambers at pressure p_2.

While $w(p_{\mathrm{SRG}})$ can be evaluated as a type-A standard uncertainty directly as the relative standard deviation of measured values, $w(p_{\mathrm{ref}})$ cannot be determined in this way. To take into account a correlation of temperature measurements of the large chamber at two successive expansions, T_2^{n-1} and T_2^n, we can express T_2^n as $T_2^n = T_2^{n-1} + \Delta T_2^n$. Here, ΔT_2^n is a change of mean temperature of the large chamber, which is typically less than ± 0.03 K. The ratio of the large chamber temperatures in Equation (3.4) can then be expressed as

$$\frac{T_2^n}{T_2^{n-1}} = \left(1 + \frac{\Delta T_2^n}{T_2^{n-1}}\right) = (1 + \delta_T), \tag{3.6}$$

where δ_T is the relative change of the large-chamber temperature. Equation (3.4) is then modified to

$$p_2^n = \frac{p_1^n}{R}\frac{T_2^n}{T_1^n} + \left(1 - \frac{1}{R}\right) + (1 + \delta_T)\, p_2^{n-1}. \tag{3.7}$$

From Equation (3.7) and following the EA guidelines [37], standard uncertainty $u(p_{\mathrm{ref}})$ can be calculated as

$$u(p_{\mathrm{ref}}) \equiv u(p_2^n) = \sqrt{w(p_1^n)^2 + w(R)^2 + w(T_2^n)^2 + w(T_1^n)^2} \cdot \frac{p_1^n}{R}\frac{T_2^n}{T_1^n} + \\ + \sqrt{\left(\frac{u(R)}{R^2 - R}\right)^2 + w(1 + \delta_T)^2 + w\left(p_2^{n-1}\right)^2} \cdot \left(1 - \frac{1}{R}\right)(1 + \delta_T)\, p_2^{n-1}. \tag{3.8}$$

Since temperatures T_2^n and T_1^n in Equation (3.8) are similar, their temperature ratio is close to 1. Furthermore, since R is very large, the terms with R^2 in the denominator are negligible as well. Taking into account that $(1 - 1/R) \approx 1$ and $(1 + \delta_T) \approx 1$, Equation (3.8) can then be simplified to

$$u(p_{\mathrm{ref}}) \equiv u(p_2^n) = \sqrt{w(p_1^n)^2 + w(R)^2 + w(T_2^n)^2 + w(T_1^n)^2} \cdot \frac{p_1^n}{R} + \\ + \sqrt{w(1 + \delta_T)^2 + w\left(p_2^{n-1}\right)^2} \cdot p_2^{n-1}. \tag{3.9}$$

An estimate of the individual uncertainty contributions in Equation (3.9) is given in Table 3.1 for a series of expansions that are presented in Figure 3.5. One of the principal

Table 3.1: Estimated input values of Equation (3.9) for a series of expansions presented in Figure 3.5.

Quantity	Value	Comment
p_1^n	≈ 750 Pa	Nominal value
$w(p_1)$	0.030 %	Quartz Bourdon Gauge, calibrated with absolute pressure balance estimated value at 750 Pa
R	7376	
$u(R)$	1.5	
$w(R)$	0.020 %	
$w(T_2^n)$	0.023 %	Typical value of standard deviation of the mean value of 4 temperature sensors across the chamber 0.07 K (calibration uncertainty and time stability negligible compared to standard deviation)
$w(T_1^n)$	0.008 %	Combined contribution from calibration uncertainty 0.01 K, time stability 0.01 K and non-equilibrium of gas with chamber walls 0.02 K
$w(1+\delta_T)$	0.010 %	Assuming $w(\delta_T) = \delta_T$, typical value $\delta_T < \frac{0.03\ \mathrm{K}}{300\ \mathrm{K}} = 1 \times 10^{-4}$

uncertainty contributions in the primary static expansion method is the expansion ratio R. By using precise temperature sensors and pressure gauges, their corresponding terms in Equation (3.9) can be kept minimal. The uncertainty is then dictated by the ability to accurately determine the expansion ratio R. While this can be done by determining the volumes of both chambers, any additional change to the system (by either adding or removing connections, valves and additional gauges and sensors) can drastically change these values, especially for the smaller chamber.

The expansion ratio R was determined in a series of experiments directly as the ratio of the pressures before and after the expansions. In our case the pressure before the expansion was measured with a calibrated Quartz Bourdon spiral manometer, and the pressure after expansion with an in-situ-calibrated capacitive diaphragm gauge. These experiments were not in the scope of this thesis, so only final result for R and $u(R)$ are given in Table 3.1.

The standard uncertainty of the calibration of all the temperature sensors is 0.01 K. An estimate for additional uncertainty due to time stability is also 0.01 K. The small expansion chamber is fully enclosed with a massive aluminium block to maximize the temperature stability and uniformity across the chamber. The temperature of the aluminium block is measured with one temperature sensor, which is in good thermal contact with the block. This value is used as a best approximation for the initial gas temperature T_1. Additional uncertainty contribution due to non-equilibrium of the gas temperature inside the small chamber was estimated to be 0.02 K.

The temperature of the large chamber is measured with four temperature sensors, fixed to the chamber at different positions. The large chamber has a diameter of 400 mm, so small temperature gradients across the chamber can develop and the temperature values of the four sensors are slightly different. The mean value of all four temperature sensors is used as a best approximation for the gas temperature after the expansion T_2. A typical standard deviation of the mean value is 0.07 K. Compared to this value, the calibration uncertainty and long-term stability of the temperature sensors are negligible, so the relative uncertainty of T_2 is estimated to be about 0.023 %.

Relative uncertainty of the reference pressure $w\left(p_2^n\right) = u\left(p_2^n\right)/p_2^n$ slightly increases after every expansion due to temperature drifts of the large chamber (second term in

Equation (3.9)). Calculated values of $w(p_2^n)$ for a series of expansions of p_2 from 0.1 Pa to 1 Pa in steps of 0.1 Pa using Equation (3.9) with estimated values of the individual contributions from Table 3.1 is shown in Figure 3.7.

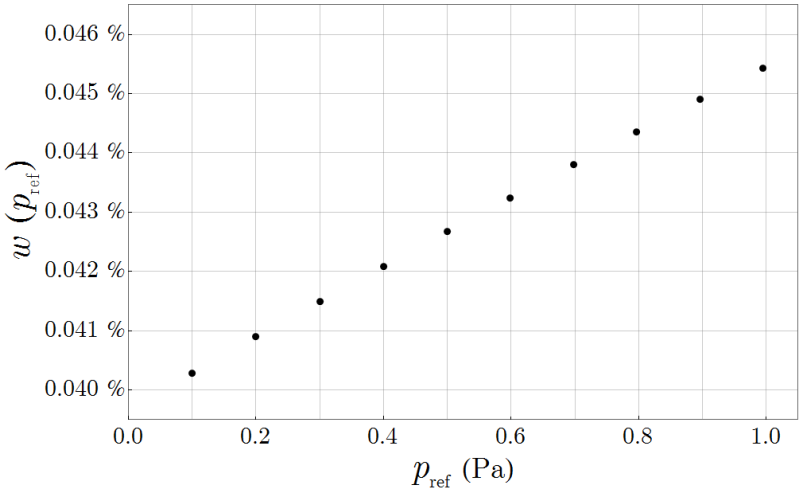

Figure 3.7: Relative standard uncertainty of reference pressure p_{ref} generated by IMT static expansion system for the same data points shown in Figure 3.5. The values were calculated using Equation (3.9) and data from Table 3.1.

The relative standard uncertainty of the SRG readings in the pressure range from 0.1 Pa to 1 Pa is below 0.01 % when a sampling interval of 10 s is used (see Chapter 4). $w(p_{\mathrm{SRG}})$ in Equation (3.5) is then only a minor uncertainty contribution and the resulting relative uncertainty of $p_{\mathrm{SRG}}/p_{\mathrm{ref}}$ is largely determined by the relative uncertainty of the reference pressure given by Equation (3.9).

After determining the relative uncertainties from Equation (3.5) for each pressure point, the expanded standard uncertainty ($k = 2$) of the ETMAC can be determined from the uncertainty of the coefficients of linear regression [41]. In our case the expanded standard uncertainty of the ETMAC was below 0.2 % in all calibrations.

As said earlier in this chapter, the IMT static expansion system is still under metrological validation. Part of this validation was also participation of the system in a laboratory comparison Euramet.M.P-K15.1 in the pressure range from 3×10^{-4} Pa to 1 Pa. Transfer standards were two SRG rotors and the measurand in the comparison was the ETMAC of the rotors. The calibration gas was nitrogen. Measurements at IMT were performed in June 2018, which was just after the first part of the study presented in Chapter 6. Pressure points 0.09 Pa, 0.03 Pa and 1 Pa in the comparison were generated by successive expansions without intermediate evacuations of the large chamber, which means by the same method developed within this PhD work. The reference pressure was calculated using Equation (3.4), and the uncertainty was estimated using Equation (3.9).

Very recently, in July 2020, draft A report of the comparison was prepared by the pilot laboratory PTB and circulated to the participants. The comparison of the IMT results and the reference values determined by the pilot laboratory at pressure points 0.09 Pa, 0.3 Pa and 1 Pa, as given in this report, are presented in Table 3.2 and also in Figure 3.8. Measurement series PTB 2 and PTB 3 were performed before and after the measurements at IMT, respectively. Deviation of IMT from the mean value of PTB measurements is less than the combined standard uncertainty ($k = 1$) of PTB and IMT, and is less than 0.1 % at 0.3 and 1 Pa. We can conclude that the IMT results in this comparison are in full equivalence with the well-established PTB primary static expansion

Table 3.2: Results of IMT obtained by a primary static expansion method and pilot laboratory PTB in the laboratory comparison Euramet.M.P-K15.1. Note*: $\mathrm{PTB_{mean}} = (\mathrm{PTB_2} + \mathrm{PTB_3})/2$.

ETMAC of rotor SRG1							
p (Pa)	PTB 2	IMT	PTB 3	$\mathrm{PTB_{mean}}^*$	IMT-$\mathrm{PTB_{mean}}$	u(PTB)	u(IMT)
0.0900	1.0722	1.0702	1.0710	1.0716	-0.0014	0.0011	0.0010
0.3000	1.0666	1.0655	1.0654	1.0660	-0.0005	0.0010	0.0009
1.0000	1.0523	1.0517	1.0507	1.0515	0.0002	0.0010	0.0010

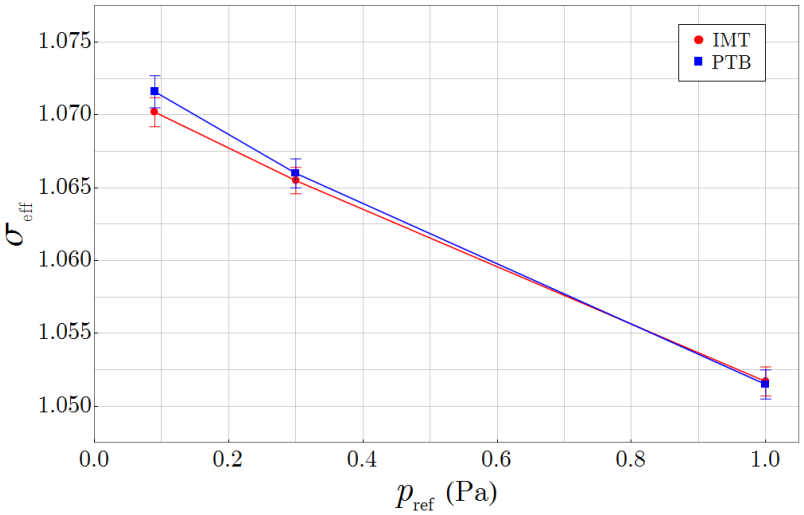

Figure 3.8: Comparison of IMT primary static expansion method with reference values of the pilot laboratory PTB in the range from 0.09 Pa to 1 Pa in the laboratory comparison Euramet.M.P-K15.1.

system and that the IMT primary static expansion system is capable of generating reference pressures with an expanded uncertainty below 0.2 % for calibrations of SRGs. The results of this comparison also validate our new procedure for generating calibration pressures by successive expansions without intermediate evacuation of the large chamber.

3.3 Pressure Decay Method

The experimental setup is shown in Figure 3.9. The conductance was determined with a pressure-decay method, where pure gas is pumped from the large chamber through the tube. Pressure was measured with either the SRG or the capacitive diaphragm gauge (CDG), where the latter was used at pressures above the the SRG's measurement range. Since the inlet pressure is much higher than the outlet pressure, the conductance is determined solely by measuring the pressure decay in the large chamber. A similar method was used by Yoshida *et al.* [12] to measure conductance of an experimental channel between two parallel disks.

When we fill the CH1 with non-adsorbing gas and let it be pumped through the tube, the pressure decreases with time. The rate of this pressure decrease is proportional to the

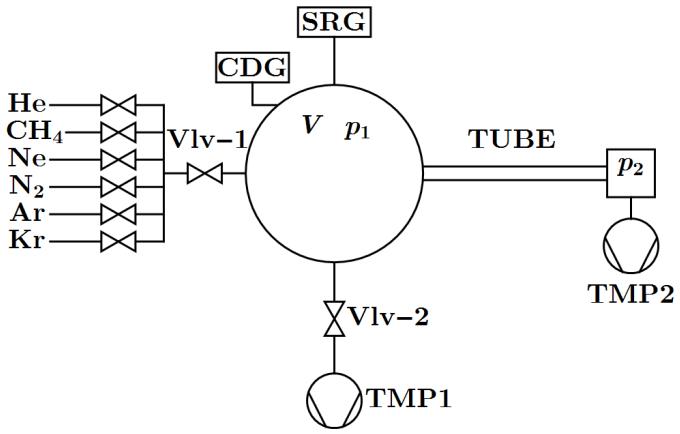

Figure 3.9: Measuring system for tube conductance measurement by pressure decay method. Vlv-1, Vlv-2 – vacuum valves , TMP1, TMP2 – turbomolecular pumps, CH1, CH2 – vacuum chambers, SRG – spinning rotor gauge, CDG - capacitive diaphragm gauge.

conductance of the tube, which is defined as [4]

$$C = \frac{V}{p_1 - p_2} \frac{\mathrm{d}p_1}{\mathrm{d}t}. \tag{3.10}$$

When the downstream pressure is negligible ($p_1 \gg p_2$), Equation (3.10) can be integrated to

$$p_1(t) = p_0 \exp\left(-t/\tau\right). \tag{3.11}$$

Here, p_0 is the initial pressure and τ is the time constant of the pressure decay, which is equal to

$$\tau = V/C. \tag{3.12}$$

In the case of molecular flow (when p_1 is sufficiently low), the conductance is pressure independent and τ has a constant value. At the transition or viscous flow, the conductance C and τ change with pressure.

It should also be noted that Equation (3.10) only considers the volume fraction of the gas that is pumped and does not include the desorption from the walls.

The logarithm of Equation (3.11) is

$$\ln\left(p\left(t\right)\right) = -\frac{C}{V}t + const. \tag{3.13}$$

It follows from Equation (3.13) that the calibration factor of the pressure gauge is contained in the constant term, and it does not contribute to the slope of the logarithm of the pressure. This is true if the calibration factor is pressure independent, or, in other words, the gauge is linear. The SRG is known to be the most linear vacuum gauge in the pressure range below 0.1 Pa. This also means that the calibration of the SRG for each gas used is unnecessary, even though the momentum accommodation coefficient of the SRG is slightly gas-dependent [24]. Independence from the gauge-calibration constant is a distinctive feature of our measurement method. There is no contribution of the calibration constant of the vacuum gauge to the uncertainty of the measured conductance as long as the SRG is used within its linear pressure range. The CDG used at higher pressures, however, is not linear, and its calibration was therefore necessary. Nevertheless, because only the low-pressure value of the ETMAC was determined for the purposes of the research

presented in Chapter 5, the uncertainties arising from calibration of the CDG were not important, since the SRG was used.

From Equation (3.13) it follows that the measured conductance of the tube C_{meas} is proportional to the slope of $\ln(p(t))$)

$$C_{\mathrm{meas}} = -V\frac{\Delta \ln(p(t))}{\Delta t}. \tag{3.14}$$

A known volume V and an accurate measurement of the pressure in CH1 as a function of time enables an accurate determination of the tube's conductance.

Conductance is proportional to $\sqrt{T_{\mathrm{gas}}}$ [4]. Different measurements were performed at a slightly different gas temperature T_{gas}, close to the nominal temperature $T_{\mathrm{nom}} = 298$ K. To compare the tube conductances at the same nominal gas temperature the measured conductances from Equation (3.14) were corrected by

$$C\left(T_{\mathrm{nom}}\right) = C_{\mathrm{meas}}\sqrt{\frac{T_{\mathrm{nom}}}{T_{\mathrm{gas}}}}. \tag{3.15}$$

The procedure to measure the conductance as a function of the inlet pressure is as follows. We first filled the large volume with a pure gas at an initial pressure $p_0 \approx 0.1$ Pa. Then we continuously recorded the pressure $p_1(t)$ every 10 s (sampling interval of SRG) while the volume was pumped through the tube down to the 10^{-5} Pa range.

The natural logarithm of pressure was then calculated, and a linear fit using the least-square method in a moving window was used to calculate the slope of $\ln(p(t))$. In our case the moving window width was chosen to be 19 points (190 s) when the gas used was helium, and 39 points (390 s) for all other gases. The width was chosen as a compromise between filtering the random noise of the pressure measurement with the SRG and the visibility of distinct features of the conductance curve.

Accurate pressure measurements with the SRG below 10^{-3} Pa require a careful offset correction of the measured values due to the pressure-independent residual drag on the spinning rotor [26]. We have also taken into account the frequency dependence of the offset correction [32]. Errors in the offset correction can introduce nonlinearities of the SRG at the lowest measured pressures.

In every vacuum system there is always some unavoidable gas source due to outgassing from the chamber walls. It is well known that in well-degassed (baked) stainless-steel vacuum systems (with metal gaskets) the dominant outgassing component is hydrogen, which is diffusing from the chamber walls.

It is easy to make a correction for the chamber outgassing with our measurement method. We closed the valve V2 at least 30 min before introducing the measurement gas. During this period the CH1 was pumped only through the tube to be measured and the residual pressure in the CH1 increased to a value of 2.5×10^{-5} Pa (H_2 equivalent), which is established as an equilibrium between the outgassing rate and the pumping speed through the tube. After introducing the measurement gas in the CH1 we obtained a gas mixture of the measurement gas and the outgassed gas, the latter being mainly H_2. In the molecular regime each gas species in the mixture is pumped independently, as there are practically no collisions between the gas molecules. This means that the partial pressure of the measured gas in the CH1 decays exponentially according to Equation (3.11), and the partial pressure of the outgassed gas remains constant, due to the constant flow into the CH1 from the chamber walls. The partial pressure of the outgassed gas is therefore simply added as an additional offset contribution to the SRG readings. The most accurate results were obtained when the SRG offset value was measured at the end of the measurement run, after the partial pressure of the measured gas dropped below 10^{-6} Pa. This offset

value was the sum of the contribution due to the residual drag on the spinning rotor and the residual pressure of the outgassed gas from the chamber walls.

The resulting conductance curve is shown in Figure 3.10; one on the untreated electropolished surface (red) and another on the oxidized surface (blue). Each curve was

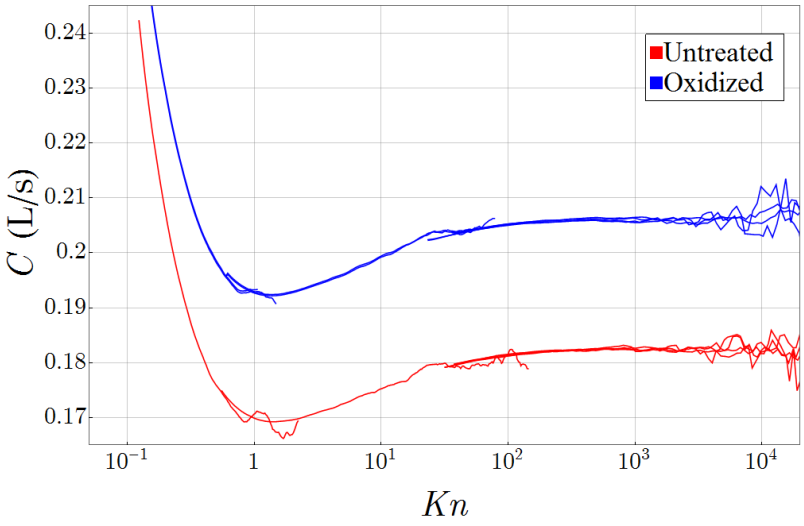

Figure 3.10: Conductance curves for He. Conductance was measured on the untreated surface (red) and again on the oxidized surface (blue). The details of the surface treatment are discussed in Section 5.1.2.

measured with He in two stages; first at pressures from 0.1 Pa down to 10^{-4} Pa, and then from 100 Pa down to 0.1 Pa. Pressure during the first stage was measured with the SRG. During the second stage, the SRG was switched off in order to prevent it from heating the measuring thimble due to re-accelerations of the rotor. The pressure in this stage was measured with two CDGs with different operating ranges; 110 Pa and 11 Pa full scale range.

3.3.1 Uncertainty of the Conductance Measurement

Following Equations (3.14) and (3.15), the relative uncertainty of the conductance C can be estimated as

$$w(C) = \sqrt{w(V)^2 + w\left(\frac{\Delta \ln(p(t))}{\Delta t}\right)^2 + \frac{1}{4}w(T_{\mathrm{gas}})^2}. \tag{3.16}$$

In our case the volume V was determined with a static gas expansion, and is known with a standard relative uncertainty $w(V) = 0.05$ %. The second term under the square root in Equation (3.16) is a result of several contributions, including the nonlinearity of the SRG. We are reporting in Chapter 5 (see Figure 3.11) only results at the characteristic Knudsen numbers $Kn > 100$, which are equivalent to gas pressures from $p < 6 \times 10^{-3}$ Pa for Kr to $p < 2 \times 10^{-2}$ Pa for He. At these gas pressures the nonlinearity error of the SRG due to gas viscosity effects is below 0.02 %, and this is negligible compared with the standard deviation of repeated measurements. The second term cannot be determined so easily from the uncertainty of the pressure measurements, so we estimate this uncertainty contribution from several repetitions of the conductance measurements at high Knudsen numbers, as shown in Figure 3.11 for argon. It should be noted that according to [4] the mean pressure in the tube, $(p_1 + p_2)/2 \approx p_1/2$, was used to calculate the characteristic Knudsen number

Kn. A typical relative standard deviation of the conductances at $Kn = 600$ is 0.13 %. The standard uncertainty of the gas temperature was estimated as $u(T_{\mathrm{gas}}) = 1$ K. This is

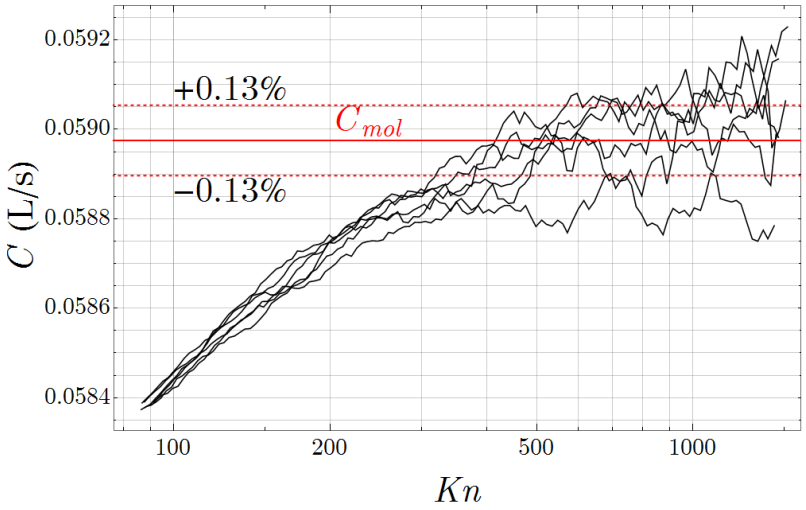

Figure 3.11: Repeated conductance measurements for Ar showing a typical statistical scatter of the measurements at high Knudsen numbers Kn.

mainly a consequence of the temperature distribution over all seven temperature sensors placed on the system; the uncertainty of the temperature sensors is negligible compared to this. Combining all three uncertainty contributions into Equation (3.16), we obtained the relative standard uncertainty of the measured conductance at the nominal gas temperature $T = 298$ K, equal to $w(C) = 0.22$ %, and the expanded relative uncertainty ($k = 2$) below 0.5 %.

Chapter 4

Origins of the Measurement Uncertainty of the Spinning Rotor Gauge

The spinning rotor gauge was used in the majority of the experimental work presented in this thesis, due to its excellent characteristics in the required pressure range, its long-term stability, and its linear response. In preparation for the work, presented in Chapters 5 and 6, special care had to be taken in order to minimize its measurement uncertainty. This chapter contains the results of this study.

4.1 Materials and Methods

In this work, a stainless-steel chamber was used. The chamber was connected to a turbomolecular pump that enabled the base pressure inside the chamber to reach below 10^{-7} Pa. In order to exclude the effects of varying gas pressure due to temperature drifts during repeated measurements, we performed measurements at the base pressure of the system, where the SRG measures only the residual drag RD.

Three MKS Instruments SRGs were used: two model SRG 2-CE (here named SRG A and SRG B), and one newer model SRG 3 (SRG C). All three SRGs were controlled remotely with a computer, which allowed for automation of the measurements. Measurements of the signal voltage were made by connecting the analog output of the SRG control unit to an oscilloscope.

For the purposes of determining the measurement precision, several measurement series were performed at different sampling intervals and at two rotor frequency ranges: 405-425 Hz and 785-805 Hz. For each measurement series 200 successive readings were recorded with all three SRGs. Measurement series were repeated at different sampling intervals 5 s, 10 s, 15 s, 20 s, 30 s, 40 s, and 60 s at the lower frequency range. Due to limited capacity of the SRG's digital counter of zero crossings, the maximum sampling interval at the nominal frequency of 800 Hz is automatically reduced by the SRG controller to around 37 s. The measurement series at the higher frequency range were therefore repeated at sampling intervals 5 s, 10 s, 15 s, 20 s, 30 s, and 37 s.

After completing each series the outliers were removed from the 200 pressure readings. This was done by removing all the readings that differed from their mean value by more than 2.5-times their standard deviation. Next, the standard deviation of the remaining readings was calculated in a moving window of 10 readings for each series. This was done in order to minimize the possible influence of temperature drifts on the measurement

precision of the SRG (term $2\alpha\frac{\mathrm{d}T_{\mathrm{rotor}}}{\mathrm{d}t}$ in Equation (1.19)). Finally, a mean value of the standard deviations obtained in this way was calculated for each measurement series.

The spinning rotors of three SRGs were then stopped, and the measuring heads were dismounted so that the rotors came into physical contact with the thimbles. The heads were then placed back and the rotors were re-suspended. The head of SRG C was simply removed from the thimble, and then placed back on. The heads of SRG A and B, however, were replaced in a different manner. First, the heads, while still on the thimble, were tilted by about 30° from vertical, and then removed from the thimble. They were then replaced vertically back on the thimble. This procedure resulted in a different orientation of the spinning rotor once re-suspended in SRGs A and B and a noticeable change of the amplitude of the induced voltage signal, while the change of orientation of the rotor of SRG C was so small that the amplitude of the induced voltage was practically unchanged. The measurements of the SRGs' precision were repeated with all three SRGs. The whole procedure was then repeated one more time.

For the analysis of the results, the standard uncertainty of the deceleration rate DCR from Equation (3.2) can be rewritten into the form for the standard uncertainty of the measured pressure value $u(p)_{\mathrm{A}}$ by applying Equation (1.18)

$$u(p)_{\mathrm{A}} = \sqrt{\frac{8k_{\mathrm{B}}T}{\pi m}}\,\frac{\pi\rho r}{10\sigma_{\mathrm{eff}}}\,\frac{32s_{\mathrm{t}}}{\sqrt{\nu}\,(\Delta t)^{5/2}}. \tag{4.1}$$

It is important to note here that $u(p)_{\mathrm{A}}$ is not the same as $u(p_{\mathrm{SRG}})$ defined in Equation (3.1), but that it represents only the type-A contribution to $u(p_{\mathrm{SRG}})$, originating from $u(DCR)$ in Equation (3.1). Standard uncertainty can be expressed as the standard deviation of repeated readings if the pressure readings follow a Gaussian probability distribution around some mean value. An example of the measured distribution of the SRG readings is shown in Figure 4.1 for SRG A at $\Delta t = 5$ s and rotor frequencies 420 Hz (red bins) and 800 Hz (blue bins). Both cases show a Gaussian distribution, meaning that $u(p)_{\mathrm{A}} = s(p)$, where $s(p)$ is

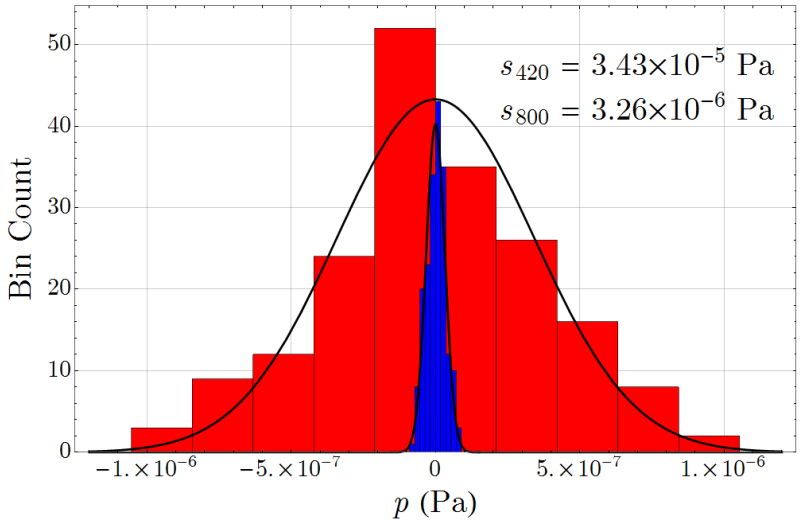

Figure 4.1: Distribution of pressure readings around the mean value at rotor frequencies 420 Hz (red bins) and 800 Hz (blue bins). Standard deviation of readings at 420 Hz s_{420} is ten times larger than the standard deviation at 800 Hz s_{800}.

the standard deviation. Furthermore, it can already be seen that the standard uncertainty at the lower rotor frequency (s_{420}) is almost ten times larger than at the higher frequency

(s_{800}), when according to Equation (4.1) this ratio should be around $\sqrt{2}$. This finding provided additional motivation for this study.

4.2 Results

The standard deviation of pressure measurements as a function of the sampling interval is shown in Figure 4.2, where SRG A, SRG B, and SRG C are individually shown in (a), (b), and (c), respectively.

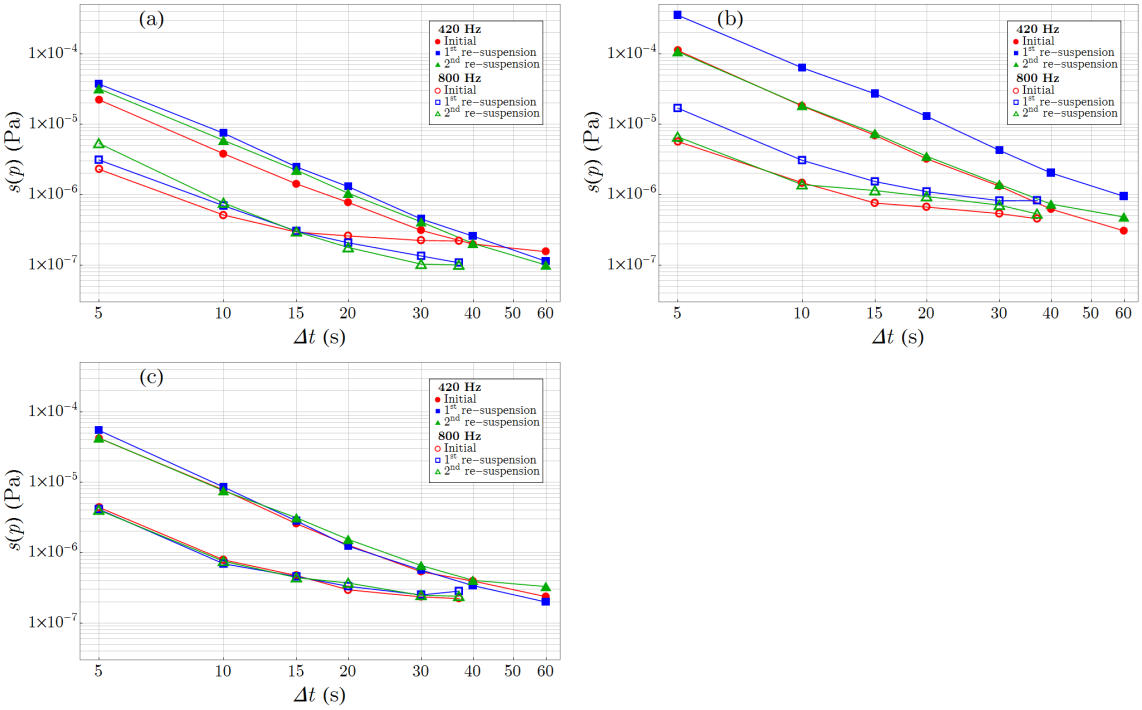

Figure 4.2: Standard uncertainty of pressure measurements for SRG A (a), SRG B (b), and SRG C (c) are shown in the logarithmic scale as a function of the sampling interval.

According to Equation (4.1) the standard uncertainty of the pressure readings should be inversely proportional to the sampling interval raised to the 2.5^{th} power. On a logarithmic scale this would appear as a linear function with a slope equal to -2.5. While the curves in Figure 4.2 might appear to be linear at low values of the sampling interval, the slope is decreased at larger values. The standard uncertainty then cannot be reduced further by simply increasing the sampling interval. This limiting value is attributed to environmental conditions, such as ambient vibrations, which cannot be easily dampened. Furthermore, this limit can change even between re-suspension of the rotors, as was the case for SRG A after first re-suspension. If the slope is calculated only for $\Delta t = [5\text{ s}, 10\text{ s}]$ its value is shown to be near the ideal value -2.5. The calculated slopes are shown in Table 4.1. Deviations from the ideal value occur due to the previously described lower limit of uncertainty.

The standard uncertainty of pressure measurements is strongly affected by the rotor frequency. At 800 Hz the standard uncertainty should be lower to the standard uncertainty at 420 Hz by a factor of about $\sqrt{2}$, according to Equation (4.1). However, it can be clearly seen in Figure 4.2 that it was about 10-times lower for small values of the sampling interval. This ratio became smaller at larger values, but this is the consequence of the lower limit of the measurement uncertainty, as discussed previously.

Table 4.1: Slopes of the curves shown in Figure 4.2 calculated for small values of the sampling interval (5 s and 10 s). Deviations from the expected value -2.5 occur due to flattening of the curve at higher values of the sampling interval.

	420 Hz			800 Hz		
	Initial	1st re-suspension	2nd re-suspension	Initial	1st re-suspension	2nd re-suspension
SRG A	-2.55	-2.32	-2.44	-2.16	-2.16	-2.81
SRG B	-2.63	-2.48	-2.54	-1.94	-2.46	-2.25
SRG C	-2.45	-2.68	-2.49	-2.48	-2.57	-2.42

Re-suspension of the SRG rotor can greatly affect its standard uncertainty. The largest change occurred after the first re-suspension of the rotor of SRG B. After the second re-suspension, however, its standard uncertainty returned to near initial values. On the other hand, if re-suspension is done carefully, such as was our procedure with SRG C, or the rotor is just stopped and re-suspended without removing the measuring head, the standard uncertainty should keep previous values.

s_t in Equation (4.1) is the standard uncertainty of the measured time intervals between zero crossings of the signal voltage of the SRG, which should be unaffected by the sampling interval at a given rotor frequency. As can be seen in Figure 4.3, however, this was not the case. Here, s_t was calculated from $u(p)_A$ with the help of Equation (4.1). While for

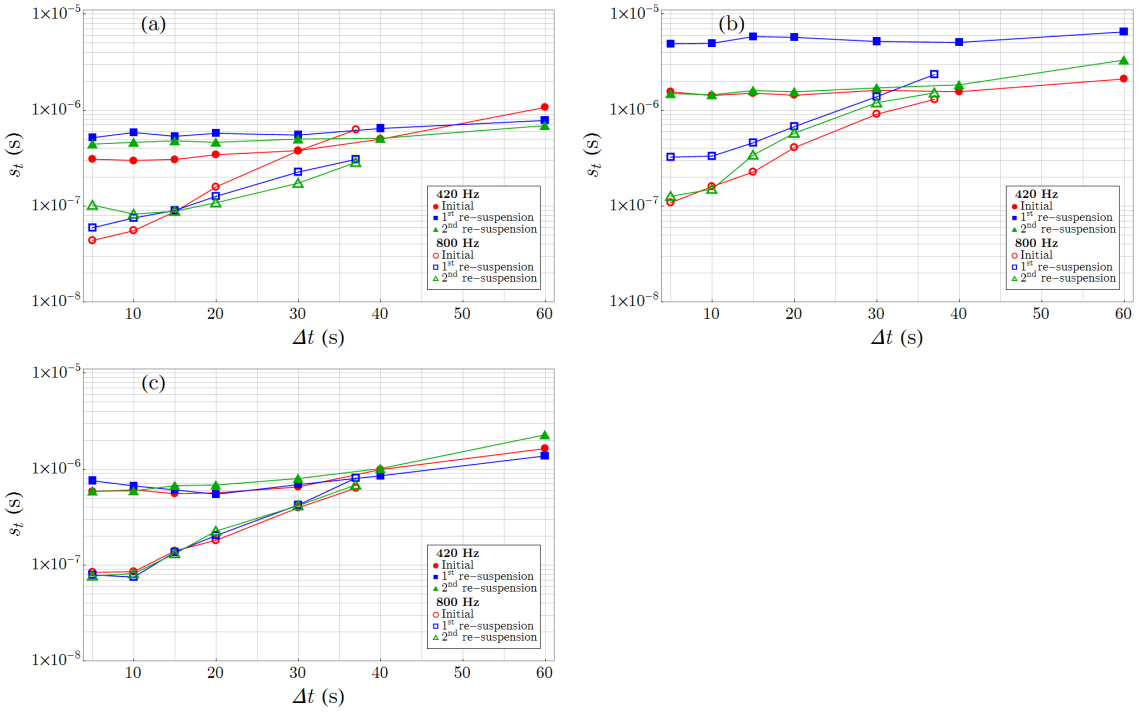

Figure 4.3: The uncertainty of the measured time intervals of the signal voltage of the SRG. The uncertainty should remain constant for all values of the sampling interval, however it appears to have increased due to environmental effects at higher values.

low values of the sampling intervals s_t appeared constant, its value increased at larger values of the sampling interval. This is again due to environmental factors unrelated to the SRG's measurement of the rate of decay of the rotor frequency, which means that the

values presented in Figure 4.3 do not accurately depict the true value of s_t.

The reason for a large difference in s_t for rotor frequencies 420 Hz and 800 Hz is not immediately apparent. It can, however, be explained by observing the signal voltage induced in the pickup coils of the SRG. This is shown in Figures 4.4, 4.5, and 4.6 for SRG A, SRG B, and SRG C, respectively. In the simplest case the induced voltage is a sine wave

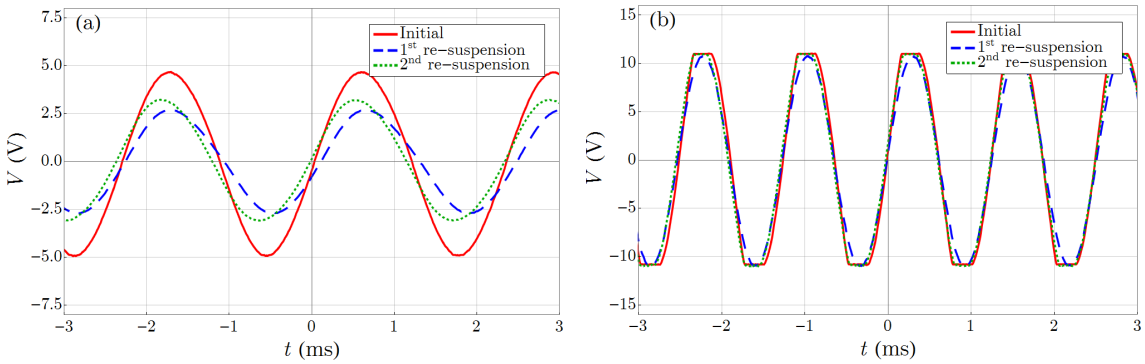

Figure 4.4: Signal voltage of SRG A recorded with an oscilloscope at 420 Hz (a) and at 800 Hz (b).

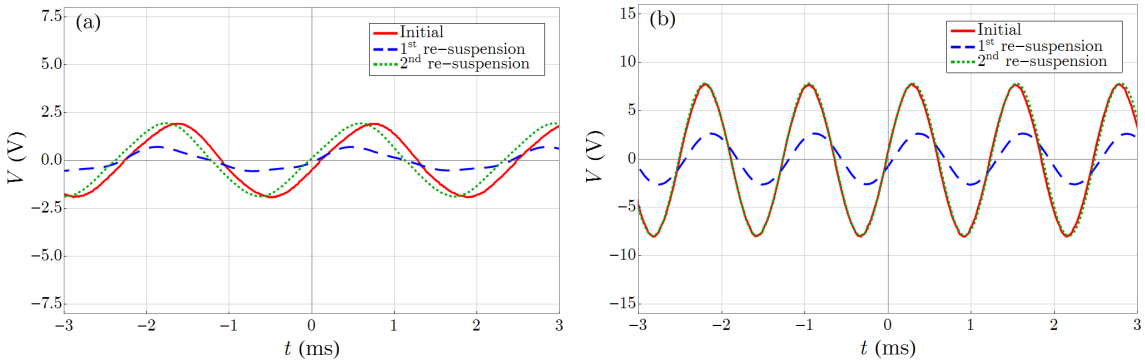

Figure 4.5: Signal voltage of SRG B recorded with an oscilloscope at 420 Hz (a) and at 800 Hz (b).

(unless its amplitude is larger than the cut-off value determined by the electronics of the SRG, as is the case for SRG A and SRG B at 800 Hz in Figure 4.4 (b) and Figure 4.6 (b)).

A magnified view of the zero crossing for the case of SRG A during the initial measurement series is shown in Figure 4.7 (a). The uncertainty of the voltage output depends on the noise of the induced voltage signal in the pickup coils and the electronics involved in the voltage measurement and should be independent of the working parameters of the SRG. When the slope of the voltage signal is larger, as was the case at 800 Hz (blue dashed line), s_t must be smaller. The inverse relationship of the slope and s_t is therefore expected. This is supported by multiplying s_t and its corresponding value of the slope of the voltage signal k given in Figure 4.7 (a). The products (which are proportional to the uncertainty of the voltage output) are very close for both frequencies. This relationship is shown in Figure 4.7 (b). Here, data points for the sampling intervals 5 s and 10 s were chosen. The presented data shows that s_t follows the power law

$$s_t \propto \left(\left| \frac{\mathrm{d}V}{\mathrm{d}t} \right|_{V=0} \right)^{-\gamma}, \tag{4.2}$$

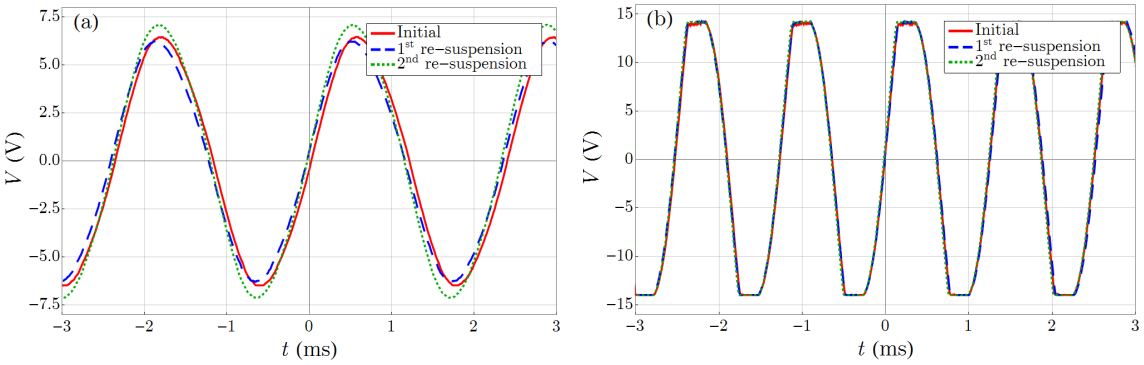

Figure 4.6: Signal voltage of SRG C recorded with an oscilloscope at 420 Hz (a) and at 800 Hz (b).

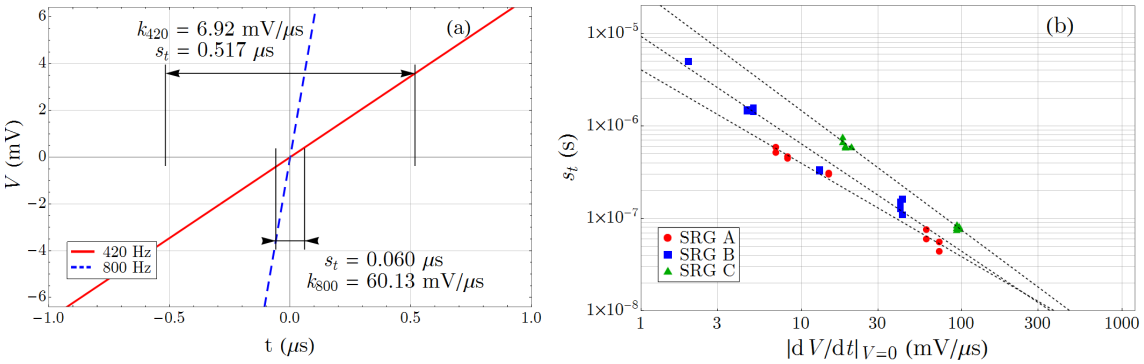

Figure 4.7: The inverse relationship between the slope of the voltage signal at zero voltage and s_t is shown with the initial signal voltage data of SRG A, where s_t and the slope of the voltage k are also given (a). Uncertainty of transition times as a function of the slope of the voltage signal at zero voltage (b). Data points for sampling intervals 5 s and 10 s are combined and shown for each SRG individually. The dashed lines are linear regressions of the data points.

and linear regression reveals values of γ for SRG A, SRG B, and SRG C to be 1.010, 1.162, and 1.292, respectively.

4.3 Discussion

As discussed previously, the induced voltage signal is a consequence of the rotating component of the rotor's magnetic moment. When the rotor is stationary and magnetically suspended, it tends to orient itself so that its magnetic moment is parallel to the external magnetic field. However, its moment of inertia is usually not parallel to the magnetic moment, and a spinning rotor tends to align its moment of inertia with the axis of rotation. The torque resulting from this is a function of the rotor's frequency. This torque competes with the one resulting from the magnetic moment, which leads to the fact that the inclination angle of the magnetic moment changes with the rotor frequency [28], which leads to a change in the amplitude of the AC voltage signal induced in the pickup coils of the SRG.

The induced voltage has a small amplitude and is together with the noise further amplified in the electronic circuit in order to get a usable signal for the frequency measurement.

The signal-to-noise ratio of the detected voltage determines the precision of the rotor deceleration measurement. Assuming that the noise is a characteristic of the electronic detection circuitry and does not depend on the orientation of the rotor and its frequency, the signal-to-noise ratio can be improved by increasing the amplitude of the induced voltage signal. The SRG controller has an output connector which offers a possibility to monitor the amplified voltage signal from the detecting coils using an oscilloscope. When the amplitude of the detected voltage exceeds a certain level, the amplifier gets saturated and the amplified sine-wave form is clipped. However, the slope of the sine-wave curve at the transition through the zero level is proportional to the amplitude, and in the region of zero transition the amplifier is not at saturation. Actually, for measurement of the rotor frequency, a section of the detected voltage around zero crossing is used [27], [29].

We discovered in this study that the main characteristic that determines the Type-A measurement uncertainty of the SRG is the steepness of the zero crossing, i.e., the slope of the induced signal voltage at the transition through zero level. We also found that increasing the rotor frequency from 420 Hz to 800 Hz significantly increases the amplitude of the detected voltage signal in the pickup coils. As a result, the slope of zero crossing is also significantly increased, which leads to a reduced Type-A measurement uncertainty (standard deviation of measured values) of the SRG.

If the induced signal voltage and consequently the slope of the zero crossing is too small to achieve the required standard deviation, it can be altered in several ways. The simplest way is to increase the rotor frequency. The resulting slope of the voltage signal is therefore increased, since the slope is proportional to the rotor frequency, as well as the amplitude of the voltage signal. We have found in our study that at a sampling interval of 10 s or less the standard deviation is reduced by a factor approximately 10 when the frequency is increased from 420 Hz to 800 Hz.

If the rotor frequency cannot be increased (due to the resulting necessity for a frequency correction of the residual drag, as discussed in Section 3.1.1), the magnetic suspension can be terminated, the suspension head removed, and then reinstalled in a way that the rotor has a different orientation with respect to its moment of inertia. This will change the amplitude of the induced voltage signal, with the possibility of increasing or decreasing it. So it may be necessary to repeat the procedure several times until a signal of sufficient amplitude is achieved.

Finally, if all else fails, the magnetic moment of the rotor can be changed by exposing it to a stronger magnetic field. This can drastically change its magnetic moment and a danger exists that the rotor is magnetized too much. In such a case the consequence will be a significantly increased residual drag and also its frequency dependence. One possibility to de-magnetize a rotor is a bakeout to high temperature, but this will also affect its momentum-accommodation coefficient (see chapter 6), and a re-calibration may be necessary.

Chapter 5

Influence of Surface Conditions on the Tube's Conductance

The aim of this work was to investigate the influence of different treatments of the technical surface of a long tube made from stainless steel on the conductance of the tube in the molecular flow regime. Stainless steel is the most common material for vacuum chambers and components, and the two extremes of macroscopic surface roughness, i.e., (i) the electropolished surface representing a very flat surface and (ii) the chemically etched surface representing very rough surface, were studied. The results as presented here were published in the international journal Vacuum [7].

5.1 Materials and Methods

5.1.1 Measuring System

A dedicated vacuum system for tube-conductance measurements using the pressure-decay method in the molecular and transition regimes was built in our laboratory. A schematic view of our measurement setup is shown in Figure 3.9.

The tube for which the conductance is to be measured is connected between two vacuum chambers, CH1 and CH2. Here, CH1 is the large chamber of a primary static expansion calibration system. The volume of CH1 was determined using the static gas expansion method [42], [43] from another chamber, the volume of which was determined gravimetrically by measuring the mass of the empty chamber and the mass of the same chamber filled with deionized water. The volume of CH1 was determined prior to attaching the tube to be measured with the connection port closed with a blank flange. The small change of volume after attaching the tube was determined from the geometrical measurements of the connecting fitting.

The volume of CH1 with the tube fitting is $V = 37.012\ \mathrm{L} \pm 0.02\ \mathrm{L}$. CH1 can be evacuated with a turbomolecular pump TMP1, having a pumping speed of 80 L/s for N_2. Chamber CH2, with a volume of approximately 5 L, is directly connected to a turbomolecular pump TMP2, having a pumping speed of 220 L/s for N_2.

Gases of purity 99.999 % are introduced into CH1 via valve V1 from gas cylinders through an all-metal gas-delivery system. The pressure inside the CH1 is measured with a spinning rotor gauge (SRG) in the range from 10^{-1} Pa down to 10^{-5} Pa.

The tube to be measured was carefully selected to have a well-defined roundness and a very uniform cross-section along the length. The selected sample tube was manufactured by the company Dockweiler AG, grade ULTRON, with an outer diameter of 9.53 mm (3/8 in). The tube is made of 316L stainless steel with an electropolished finish on the inner surface.

Three samples of length 1 cm, 780 cm and 1 cm were cut consecutively from a longer piece of the tube. The shorter samples were used for measurements of the roundness and the inner diameter, which were made by the Slovenian national laboratory for dimensional measurements, using a coordinate-measuring machine. The longer sample was machined to a length $L = 777.0\ \text{mm} \pm 0.1\ \text{mm}$. All the cutting and machining was conducted carefully in order to preserve the roundness of the samples. The results of the diameter measurements on both short samples gave a mean value of $d = 7.768\ \text{mm} \pm 0.002\ \text{mm}$. The diameters of the tube near both ends were equal to within 0.03 %. With the available dimensional measurement equipment we could not check the uniformity of the tube's inside diameter along the length. But we were able to determine the mean inside diameter of the whole tube by measuring gravimetrically the volume of the tube. This was done by measuring the difference between the mass of the tube filled with deionized water and the mass of the empty tube. The calculated diameter from the measured volume was $d = 7.769\ \text{mm} \pm 0.005\ \text{mm}$. The relative difference of the dimensional measurement of the tube's inner diameter and the calculated mean diameter from the gravimetric measurement was less than 0.02 %. This gave us confidence about the uniformity of the tube's inner diameter.

The chamber CH2 is pumped with a turbomolecular pump that has a pumping speed much larger relative to the conductance of the tube, so the outlet pressure of the tube p_2 is much smaller than the inlet pressure p_1. The pressure ratio depends on the gas used, as the pumping speed of the turbomolecular pump does not scale with the square root of the molar mass of the gas, but in any case the pressure ratio was $p_1/p_2 > 2000$.

There are seven Pt100 temperature sensors attached to the system, five on the CH1, and two on either end of the tube. This allows for accurate temperature measurements of the gas entering the tube. Furthermore, the tube itself is covered with an aluminium shell, in order to enhance the heat transfer and therefore minimize the temperature gradients along the tube.

5.1.2 Surface Treatments

In this work we investigated the changes to a tube's conductance after different heat treatments of the tube's inner surface. During these heat treatments the two Pt100 sensors (see Section 5.1.1) were removed and three K-type thermocouples were fixed to the outside surface of the tube: two near the ends and one in the middle. They were used to control the heating temperature. Then, the tube was covered with an aluminium shell, around which a heating ribbon was wrapped. This was then wrapped in aluminium foil to ensure a homogenous temperature of the tube during heating.

The conductance of an untreated, electropolished tube was determined first for helium, nitrogen and argon. The tube was then vacuum baked at 573 K (300 °C) over 24 hours, and the conductance was determined again for argon and nitrogen.

After this stage additional heat treatments were made on the inner surface of the tube:

a) heating to 573 K with exposure to pure oxygen,

b) vacuum bake at 573 K,

c) heating to 573 K with exposure to pure hydrogen.

The oxygen for the treatment a was chosen in order to simulate a leak in a vacuum system, since the presence of oxygen from the air might introduce an oxide layer on the inner surfaces of the system. A pressure of 0.1 Pa was the maximum pressure that we could obtain with our capillary leak for the oxygen supply. Later, in treatment c, hydrogen was introduced in order to promote the reduction of the oxide through a chemical reaction to form water molecules. During the bake-out of a leak-tight vacuum system there is a significant partial pressure of hydrogen in the system because of the diffusive degassing of

dissolved hydrogen from the bulk. So this treatment step was introduced to simulate the conditions during the vacuum bake-out of the chamber as an indication of whether some changes can occur.

Each treatment was made over 24 hours. Since no valve was available at the pumping end of the tube, a constant gas flow was established for treatments a and c at an inlet pressure of 0.1 Pa, but near the outlet it was much lower, because due to continuous pumping the pressure uniformly decreased along the length to the 10^{-5} Pa range.

Three gases were added for the conductance measurements: methane, neon and krypton. Thus, the conductance was determined for all six gases after every step.

After the first set of measurements (I1, a1, b1, c1, where a, b and c indicate the treatments steps from the list above, and I indicates the initial state) the system was vented for 24 hours with room air at around 45 % relative humidity, with the expectation being to revert the tube's surface to the "as-received" state, and the whole cycle was repeated (I2, a2, b2, c2). This was done in order to test the reproducibility of the method.

Finally, the tube was removed from the measurement system and the inner surface was etched in *aqua regia* (1:3 molar ratio of HNO_3 and HCl) for 8 minutes. Surface images of coupon samples exposed to the same treatment were recorded with a scanning electron microscope to visualize the differences in the surface roughness. A comparison is shown in Figure 5.1. In addition to the SEM, the surface was imaged with an atomic force

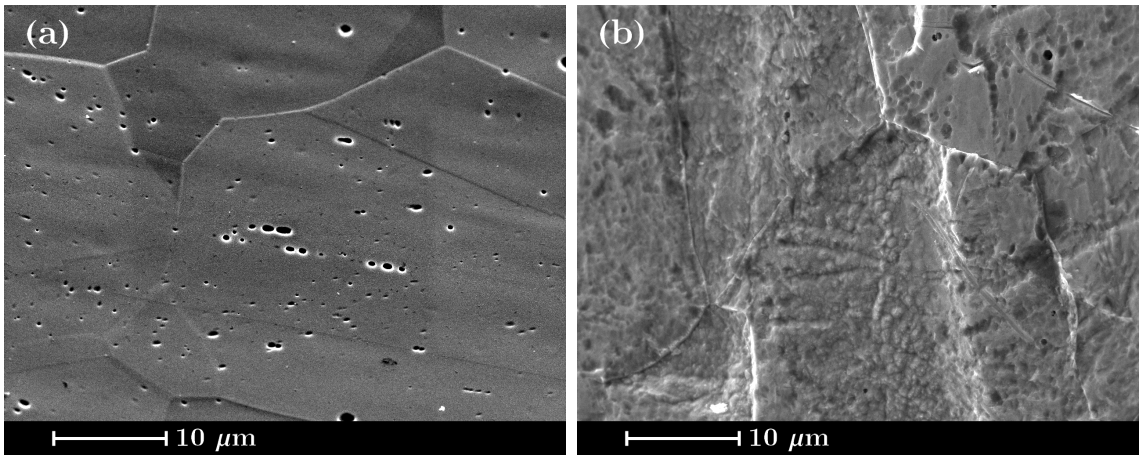

Figure 5.1: SEM images of the inner surface of the tube before (a) and after (b) etching.

microscope (AFM). The results are shown in Figure 5.2. Roughness was calculated from the AFM images, as root-mean-square roughness (S_q). The values were $S_q = 4.07$ nm for the polished surface and $S_q = 59.83$ nm for the etched surface. Acid etching therefore resulted in a more than tenfold increase of S_q.

The diameter of the tube was checked by measuring the tube mass before and after the etching. The change of mass was less than the 0.01 g resolution of the mass balance, so the estimated mean diameter change after etching was less than 0.002 %.

The etched tube was re-installed in the measurement system and the whole measurement cycle, including all the treatment steps (I3, a3, b3, c3), was then repeated for all six gases.

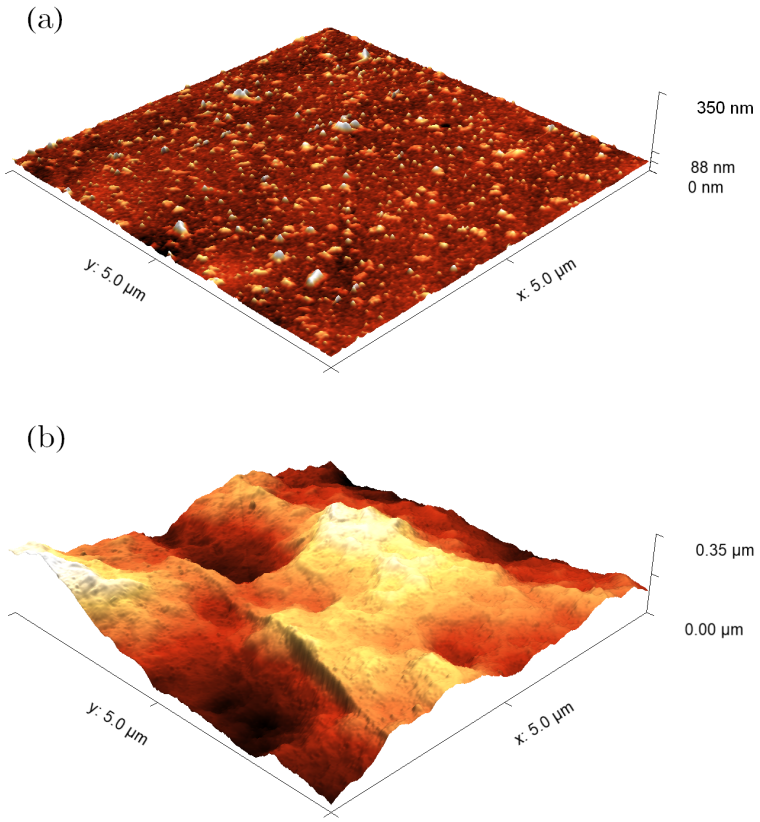

Figure 5.2: AFM images of the inner surface of the tube before (a) and after (b) etching.

5.2 Results and Discussion

Our measurements showed that there is still a deviation of the measured conductance from the free molecular limit of -0.3 % at $Kn = 200$ (see Figure 3.11). Therefore, we use the conductance at $Kn = 600$ for a comparison of the different surface treatments. At $Kn = 600$ the pressure dependence of the conductance becomes negligible, which signifies molecular flow.

The initial conductance measurements of the electropolished tube after a few days in vacuum at room temperature were made for He, N_2, and Ar. The results at $Kn = 600$ are given in the first column in Table 5.1 (I1).

The tube was then vacuum baked at 573 K for 24 hours. The change in the conductance was checked for N_2 and Ar. The results are given in the second column in Table 5.1 (vacuum bake). A simple vacuum bake did not produce a significant change in the conductance for N_2 and Ar (less than 0.2 %).

Next, treatments a - c (described in Section 5.1.2) were repeated twice, with intermediate exposure to room air between the two cycles. The conductance measurements were made after each step for He, CH_4, Ne, N_2, Ar, and Kr. The molecular conductance after each step is shown in Table 5.1 (please note that the initial values, which are given in the first column, were determined only for He, N_2, and Ar). The repeated values in cycle 2 are in good agreement with cycle 1, with a relative difference of less than 0.2 % for all the gases, except He. For He the difference between the initial values is about 2.7 % (columns I1 and I2 in Table 5.1). However, compared to the more than 10 % increase after the first heating step (a1 or a2), this can still be considered as acceptable reproducibility. The

Table 5.1: Measured conductance (at $Kn = 600$) for untreated (I1) tube and after every treatment. Second repetition consists of the same treatments as the first, with the exception of the first vacuum bake (see text for description of the treatments).

	C_{mol} (L/s); $Kn = 600$, $T = 298$ K				
	First repetition				
Gas	Initial (I1)	Vacuum bake	Oxygen bake (a1)	Vacuum bake (b1)	Hydrogen bake (c1)
He	0.1818	/	0.2054	0.2135	0.2077
CH_4	/	/	0.0939	0.0944	0.0943
Ne	/	/	0.0895	0.0902	0.0899
N_2	0.0706	0.0705	0.0720	0.0727	0.0723
Ar	0.0583	0.0584	0.0609	0.0614	0.0608
Kr	/	/	0.0417	0.0417	0.0417
	Second repetition				
Gas	Initial (I2)	Oxygen bake (a2)	Vacuum bake (b2)	Hydrogen bake (c2)	
He	0.1868	0.2074	0.2129	0.2067	
CH_4	0.0925	0.0940	0.0941	0.0935	
Ne	0.0843	0.0901	0.0906	0.0895	
N_2	0.0707	0.0722	0.0722	0.0717	
Ar	0.0582	0.0608	0.0611	0.0604	
Kr	0.0403	0.0417	0.0417	0.0413	

differences between the repeated measurements of the heat-treated electropolished surface for He (a1-a2, b1-b2, c1-c2) are also less than 1 %, which can be deemed consistent with other gases. Due to the good reproducibility, the average values of both repetitions on the electropolished surface (where available) are used in the remainder of this investigation. These values are indicated with an index m ($\mathrm{I_m}$, $\mathrm{a_m}$, $\mathrm{b_m}$, and $\mathrm{c_m}$).

After the reproducibility of the results for the electropolished surface was tested, the tube's inner surface was chemically etched, and the conductance measurements were repeated after the same heat treatments as before. A comparison of the tube conductances for the electropolished and etched surfaces is presented in Table 5.2 and Figure 5.3. For better clarity of the changes, the scaled conductance is shown in Figure 5.3. Here, the conductance is multiplied by the square root of the molecular mass of the gas being used.

A significant increase in the conductance of the electropolished tube is clearly visible for all the gases after heat treatment in oxygen ($\mathrm{a_m}$). This is most notable for He, which shows a 13 % increase. Note that for this large increase the exposure to oxygen at 573 K seems to be necessary (vacuum baking at 573 K before treatment a1 caused an almost negligible change of 0.25 % for the Ar conductance (see Table 5.1), while a subsequent oxygen bake produced a 5 % increase in the Ar conductance). The temperature of 573 K during all of our heat treatments of stainless steel is too low to cause any structural changes in the material or on the surface (recrystallization, change of surface roughness, etc.). However, the presence of oxygen at 573 K might promote the removal of carbon-containing surface contaminants that are adsorbed during handling in the atmosphere. It is well known from the field of Auger spectroscopy that any sample that is brought into the apparatus from the atmosphere maintains a considerable carbon contamination on the surface, even after it is pumped down to 10^{-8} Pa or below. Also, prolonged pumping in an extremely high vacuum does not remove the carbon contamination, although it can be removed by Ar sputtering,

Table 5.2: Measured conductances (at $Kn = 600$) of the electropolished and etched tubes exposed to various heat treatments for six different gases (see text for description of the treatments).

	C_{mol} (L/s); $Kn = 600$, $T = 298$ K			
	Electropolished			
Gas	Initial (I_m)	Oxygen bake (a_m)	Vacuum bake (b_m)	Hydrogen bake (c_m)
He	0.1843	0.2064	0.2132	0.2072
CH_4	0.0925	0.0939	0.0943	0.0939
Ne	0.0843	0.0898	0.0904	0.0897
N_2	0.0706	0.0721	0.0724	0.0720
Ar	0.0583	0.0609	0.0612	0.0606
Kr	0.0403	0.0417	0.0417	0.0415
	Etched			
Gas	Initial (I3)	Oxygen bake (a3)	Vacuum bake (b3)	Hydrogen bake (c3)
He	0.1521	0.1490	0.1496	0.1509
CH_4	0.0767	0.0761	0.0757	0.0756
Ne	0.0686	0.0675	0.0671	0.0676
N_2	0.0583	0.0578	0.0572	0.0575
Ar	0.0487	0.0483	0.0477	0.0480
Kr	0.0335	0.0333	0.0330	0.0332

which is common practice in Auger spectroscopy for surface cleaning. We can conclude that heating of an electropolished surface at 573 K in a low pressure of oxygen (0.1 Pa) produces an atomically cleaner surface, where we can expect more specular reflections [6], and consequently a higher tube conductance (Equation (1.17)).

Etching, on the other hand, produced a much rougher surface (as seen in Figure 5.1), which resulted in a much reduced conductance.

The ETMAC was calculated from the measured conductances as [7]

$$\sigma_{\text{eff}} = \frac{2PC_0}{C + PC_0}. \tag{5.1}$$

For our circular tube we have $L/R = 200.05 \pm 0.10$ and we estimated the transmission probability $P = 0.012945 \pm 0.000010$ based on the work of Gómez-Goñi and Lobo [44].

The relative expanded uncertainty of the transmission probability is ($W(P) < 0.1$ %), and is therefore small compared to the relative expanded uncertainty of our tube-conductance measurement ($W(C) < 0.44$ %). So the relative expanded uncertainty of the calculated ETMAC can be estimated as ($W(\sigma_{\text{eff}}) < 0.5$ %).

The ETMAC results are listed in Table 5.3 and visually shown in Figure 5.4. The relative change of σ_{eff} from the initial value measured on the electropolished surface is shown in Figure 5.5 (a).

It is evident that for the electropolished surface the largest change happened during heating in an oxygen atmosphere (treatment a_m). After that, the changes were much smaller. Furthermore, the changes were the largest for the lightest noble gases used (He and Ne). For He the ETMAC dropped by more than 5 % after heating in an oxygen atmosphere. CH_4 and N_2, on the other hand, showed the smallest change in ETMAC, below 1.5 %. Most importantly, heating in oxygen at 573 K on the electropolished surface

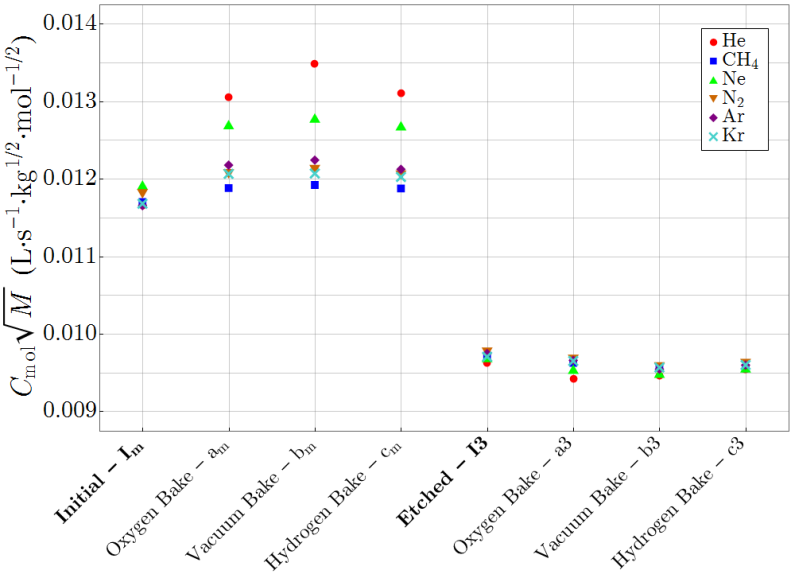

Figure 5.3: Comparison of scaled conductances (at $Kn = 600$) for electropolished ($\mathrm{I_m}$, $\mathrm{a_m}$, $\mathrm{b_m}$, and $\mathrm{c_m}$) and etched surfaces (I3, a3, b3, and c3) (see text for description of the treatments).

resulted in a decrease from the initial ETMAC for all the gases, indicating an atomically cleaner surface, which was retained after a subsequent bake in vacuum and in hydrogen.

Etching, however, resulted in a greatly increased ETMAC, about 9 % to 11 % higher for all gases. The scattering of molecules in a backwards direction (ETMAC well above 1) on the rougher (etched) surface is more probable than in the case of the smooth electropolished surface. This result is in agreement with previous studies on rough surfaces [5], [12], [24].

ETMAC variation between different gases is shown in Figure 5.5 (b). Here, data for every gas except N_2 is presented as relative difference from ETMAC of N_2. N_2 here was chosen because of its frequent use in vacuum metrology. Data therefore represents relative errors introduced to measurement, if ETMAC, which would be determined for N_2, is used regardless of the gas species present in the system. The difference before and after acid etching is clearly visible, where the variation of values on a rougher surface is much smaller (mostly below 1 %) than on a polished surface (from -4 % to 1 %).

Yoshida *et al.* [12] measured conductance of an experimental channel between two parallel disks where they varied the material and surface roughness of one of the disks. They did not find a correlation of the measured conductance on the arithmetic average roughness R_{a}, which is defined as the average height deviation from mean height of the surface (S_{q} is its 2-dimensional equivalent). However, they found the largest deviation of the measured conductance for a platinum coating with very small $R_{\mathrm{a}} = 0.010$ μm, but having a fine grain structure. They have also measured the surface profile with an AFM, and for the grainy surface of the Pt coating they found the largest slope angle of the surface elements measured with respect to the surface plane. In a very recent publication Sazhin [20] has made test particle Monte Carlo calculations of the transmission probability of a rectangular channel where he modelled a rough surface by a triangular profile of surface elements. He investigated the influence of a height r and an inclination angle of the surface micro-areas α. He found that if r is small compared to the channel height h, $r/h < 10^{-3}$, the transmission probability becomes independent of r. For our case of etched tube with measured $R_{\mathrm{a}} = 0.76$ μm (calculated from the AFM image) the relative height

Table 5.3: ETMAC values (see text for a description of the treatments).

	ETMAC σ_{eff}			
	Electropolished			
Gas	Initial (I_m)	Oxygen bake (a_m)	Vacuum bake (b_m)	Hydrogen bake (c_m)
He	1.0215	0.9647	0.9487	0.9628
CH_4	1.0194	1.0118	1.0102	1.0120
Ne	1.0102	0.9785	0.9752	0.9791
N_2	1.0150	1.0042	1.0020	1.0050
Ar	1.0215	0.9996	0.9969	1.0017
Kr	1.0204	1.0042	1.0040	1.0059
	Etched			
Gas	Initial (I3)	Oxygen bake (a3)	Vacuum bake (b3)	Hydrogen bake (c3)
He	1.1168	1.1271	1.1250	1.1207
CH_4	1.1130	1.1165	1.1190	1.1201
Ne	1.1130	1.1207	1.1234	1.1198
N_2	1.1096	1.1143	1.1192	1.1170
Ar	1.1105	1.1149	1.1208	1.1181
Kr	1.1125	1.1153	1.1197	1.1180

of surface micro-areas can be estimated as $R_a/d = 7.6 \times 10^{-7}$ m/7.77×10^{-3} m $< 10^{-4}$, so according to Maxwell [15] the measured transmission probability should be only weakly dependent on the R_a (and similarly, S_q). In our case, S_q of the etched surface was more than ten times higher than that of the polished surface. In addition to S_q, inclination distribution was calculated from the AFM images as well. This is shown in Figure 5.6. Inclination distribution on the polished and the etched surfaces has a peak at 2.6° and 7.9° inclination, respectively. Even though the transmission probability should be weakly dependent on S_q, it is strongly affected by the appearance of surface elements at higher inclination angles.

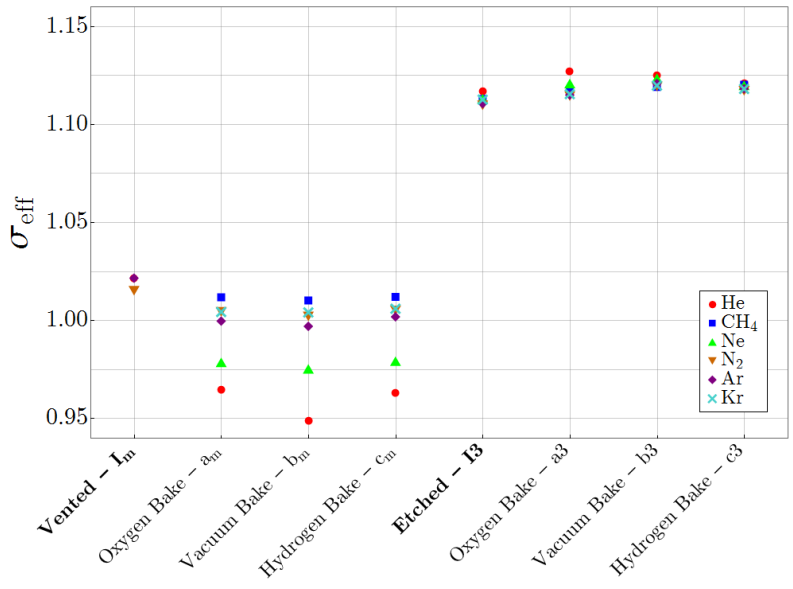

Figure 5.4: ETMAC values (see text for a description of the treatments).

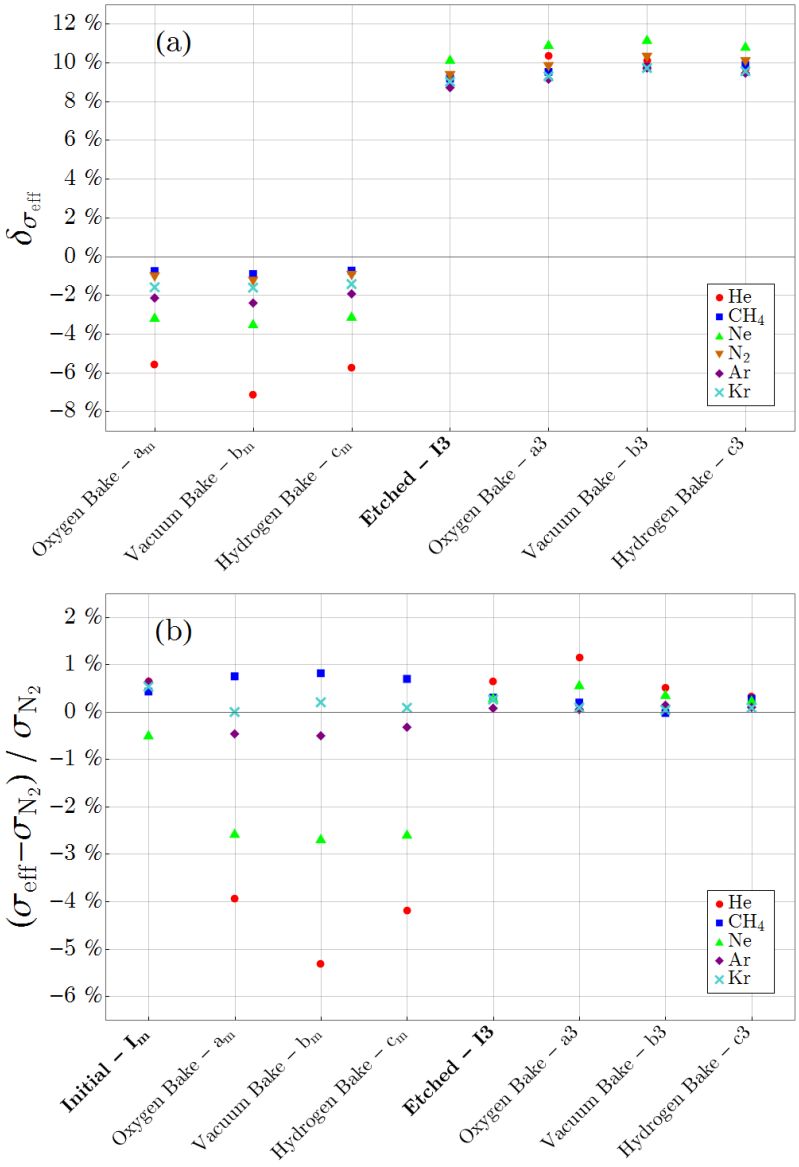

Figure 5.5: Relative change of ETMAC from the initial value (a). Change of σ_{eff} from the value for nitrogen (b). See text for description of the treatments.

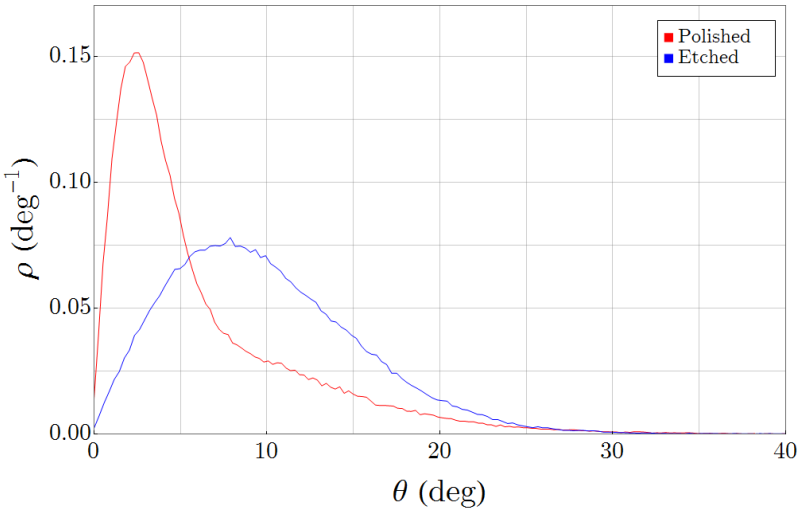

Figure 5.6: Inclination probability distribution of the polished and etched tube surface, calculated directly from AFM images.

Chapter 6

Influence of Surface Treatments of the SRG Rotors on the Momentum Accommodation

Calibration of the SRG requires determining the ETMAC of its rotor, as described in detail in Section 3.2. The aim of this work was to determine whether modifying the surface of the rotor can widen the range of applications of the SRG, in the sense of minimizing the deviations of the ETMAC on the gas species present in vacuum systems. The surface treatments chosen here were similar to those in Chapter 5 in order to determine whether different materials exhibit different patterns under similar conditions.

6.1 Materials and Methods

Three MKS Instruments SRGs were used, i.e., two model SRG 2-CE, and one model SRG 3, which allowed for the simultaneous calibration of three rotors. All three gauges were mounted directly on the same vacuum chamber. The temperature during the measurements was measured at four points across the vacuum chamber using Pt100 temperature sensors. All pressure and temperature sensors were controlled remotely with a computer, which allowed for the automation of measurements. During measurements the SRGs were operated at a rotor frequency of 405–425 Hz with a 10-seconds sampling interval. Prior to calibration, the residual drag and its frequency correction were determined, in order to minimize their contribution to the overall uncertainty.

The ETMAC was determined using the series static expansion method, as presented in Section 3.2. The expanded relative uncertainty of the ETMAC was below 0.2 % in all cases. Pressure readings were recorded simultaneously for all three SRGs at multiple pressure points between 0.1 Pa and 1 Pa. In order to check the stability of the static expansion method, one of the rotors was kept undisturbed throughout the experiment, which ensured the ETMAC remained unchanged. This rotor is marked as rotor C in the following text. Rotor C was mounted on the system a distance away from the rotors A and B, so that the high temperature during their heat treatment of other rotors did not influence the temperature of the control rotor. Rotor C was kept in a vacuum during the exposure of rotors A and B to ambient air for an extended period of time (between measurement 3 and 4). But it was exposed to the same partial pressure of oxygen at room temperature during the oxygen bake of rotors A and B.

All the rotors used here were made of 100Cr6 chrome steel as they are supplied by the manufacturer. This steel is a standard material for ball bearings. In the first part of the

study, all three rotors had a polished surface, which showed negligible surface roughness. The ETMAC was first determined for all three rotors with six gases of purity 99.999 %. The gases used were the same as in Chapter 5; He, CH_4, Ne, N_2, Ar, and Kr. Next, calibrations were repeated after two baking treatments of two of the rotors (in the following text designated as rotors A and B). The treatments chosen were vacuum bake (a) and oxygen bake (b). Both were conducted over 24 hours and at 573 K (300 °C). Treatment (a) was done at a base pressure below 10^{-6} Pa. Treatment (b) was conducted while the rotors were exposed to pure oxygen at a pressure of 10^{-2} Pa. The two rotors were then removed from the system and exposed to the atmosphere for several months. After they were replaced, treatments (a) and (b) were repeated in order to test the repeatability of the cycle. One of the rotors (rotor A) was then removed from the system. Its surface was roughened by acid etching in *aqua regia* (1:3 molar ratio of HNO_3 and HCl) for a few minutes. It was then placed back in the system and the ETMAC was again determined. Treatments (a) and (b) were repeated on the etched rotor. A summary of rotors used in this experiment is presented in Table 6.1.

Table 6.1: Summary of rotors used in this chapter. Given are their designations, surface conditions prior to treatment, and an overview of surface treatments that were applied to them. Measurement numbers, corresponding to each treatment are given in parentheses in the last column. See text for detailed description of the surface treatments.

Designation	Initial Conditions	Surface Treatments
A	polished	Cycle 1: initial (1), vacuum bake (2), oxygen bake(3). Cycle 2: air exposure (4), vacuum bake (5), oxygen bake (6). Cycle 3: etching (7), vacuum bake (8), oxygen bake (9).
B	polished	cycles 1 and 2 (treatments same as A)
C	polished	control rotor, no treatments (1-9)

Images of the modified rotors, taken with a scanning electron microscope, are shown in Figure 6.1. As was done in Chapter 5, images of these surfaces were done with the AFM, as well. They are shown in Figure 6.2. The polished surface (a) shows no outstanding features. The surface after the vacuum bake and oxygen bake (b) looks similar (a) on the SEM images. The AFM images reveal a visibly rougher surface after baking. The surface of the etched rotor E (c), reveals a very rough topology in the SEM and the AFM images, where some flat plateaus still exist (carbides in the chrome steel which are more resistant to acid etching than the surrounding structures). S_q was again calculated from the AFM images. Its value on all three surfaces is shown in Table 6.2.

6.2 Results and Discussion

Calibration curves were obtained following the method described in detail in Section 3.2. An example of the calibration curves for the rotor A in Ar gas are shown in Figure 6.3. The results show a vertical shift of the calibration curves after different treatments, while

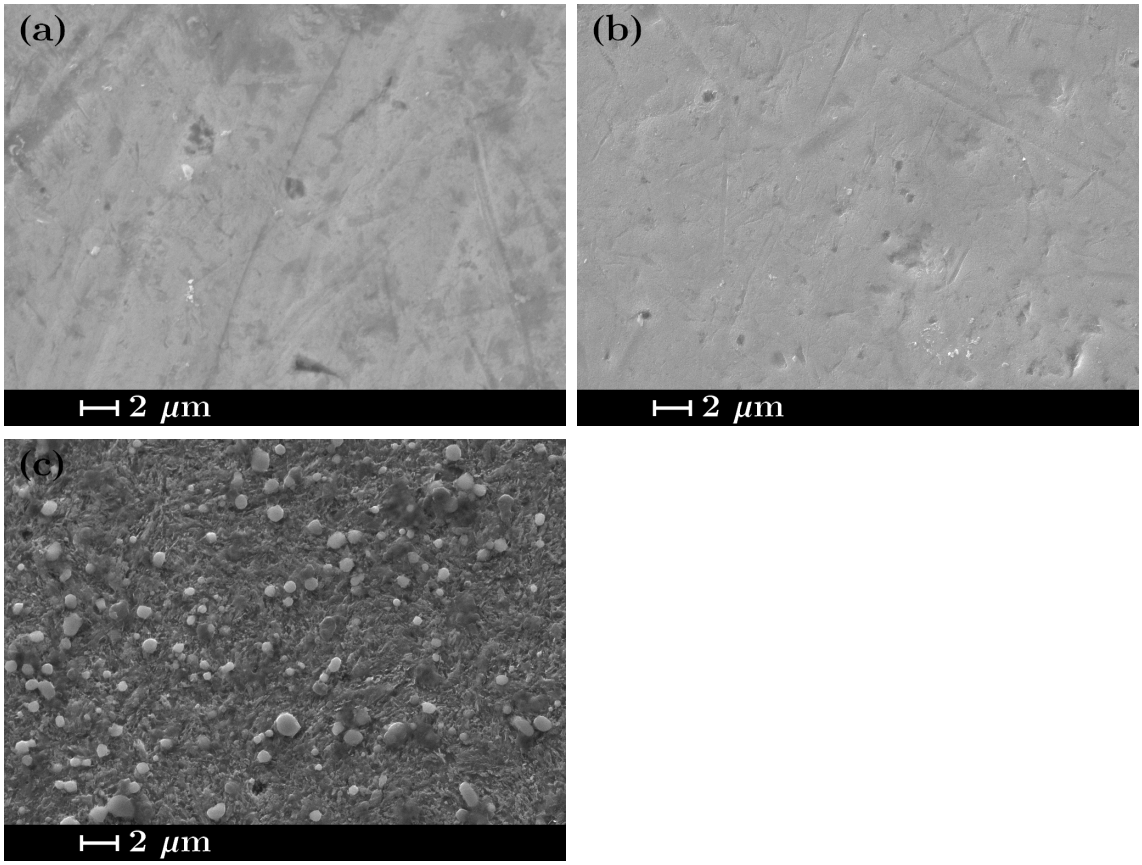

Figure 6.1: SEM images of the SRG rotors. (a) shows the polished surface. (b) shows the surface after the vacuum bake and oxygen bake steps. (c) shows the surface after roughening by acid etching. All images were taken at 10,000× magnification.

the slope of the lines was practically unchanged. The value of σ_{eff} was obtained from the intercept of y axis using linear regression.

In order to confirm that the expansion ratio remained unaffected by changes to the system throughout the experiment, the ETMAC of the rotor C was determined at every step. The results are shown in Figure 6.4. Practically all the ETMAC values of the control rotor for individual gases were within ±0.1 % throughout the experiment, which lasted for 6 months. This variation is within the estimated standard uncertainty of our calibration system and confirmed the good stability of the static expansion method. Some exceptions of larger deviation, like the about 0.3 % decrease for Kr during measurement 5, were not consistent for other gases. If during the experiment the expansion ratio was changed, due to changes made to the system, this deviation would be observed for all gases at the same measurement number. Because this was not the case, the larger change of the ETMAC is

Table 6.2: S_{q} on different SRG rotor surfaces. The values were calculated from AFM images.

S_{q} (nm)		
Polished surface	After baking	After etching
9.80	12.29	70.70

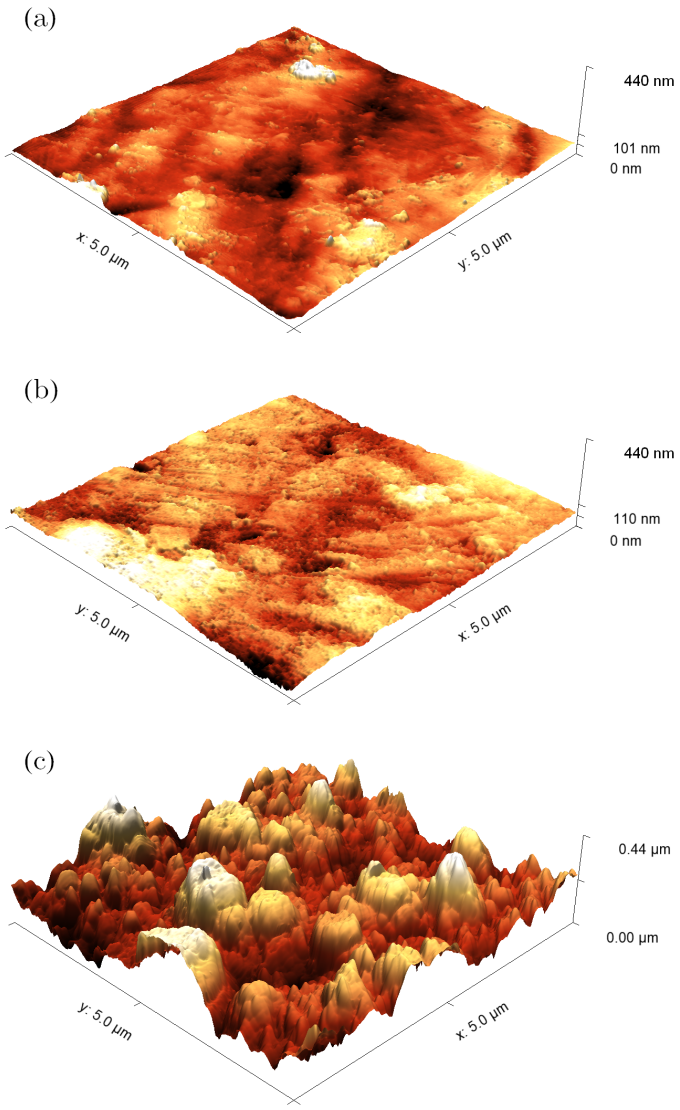

Figure 6.2: AFM images of the SRG rotors. (a) shows the polished surface. (b) shows the surface after the vacuum bake and oxygen bake steps. (c) shows the surface after roughening by acid etching.

expected to be a consequence of insufficient gas purity. This may be a result of switching between the working gases in a relatively short amount of time during the experiment, if the previous gas had not been removed completely from the gas supply line. Another possibility for the contamination of the calibration gas is the leakage of another gas into the gas supply line if the shut-off valve of that gas had not been closed completely.

The ETMAC values for all gases and the treatments of rotors A and B are shown in Figure 6.5 (a) and (b), respectively. Additionally, the ETMAC values for the polished surface of rotors A and B are presented in Table 6.3. The ETMAC values for the rotor A after etching are presented in Table 6.4, in addition to Figure 6.5 (a). Inclination probability distribution was calculated from AFM images of the polished surface, the surface after oxygen bake, and the etched surface. The results are shown in Figure 6.6.

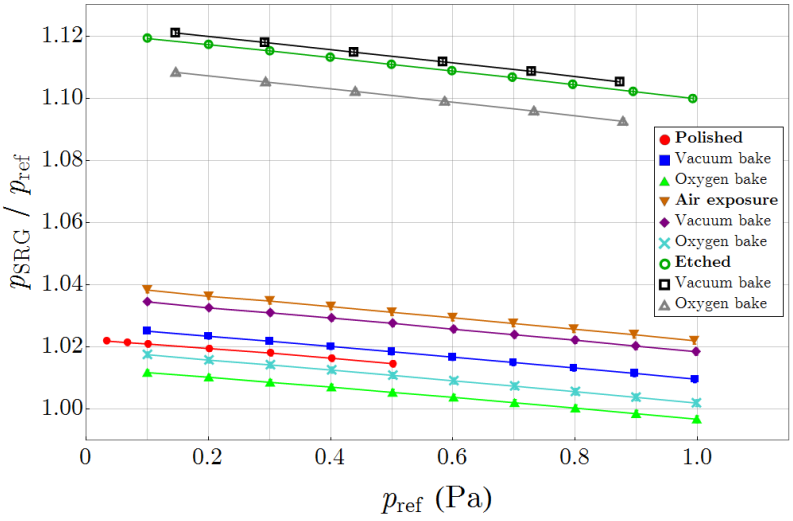

Figure 6.3: Calibration curves for rotor A. The data shown was done with Ar. ETMAC values were obtained from the y-intercept of each curve.

6.2.1 ETMAC Values of Polished Rotors After a Few Days of Pumping From Atmospheric Pressure at Room Temperature

Measurements 1 and 4 were made after a few days pumping of the rotors from atmospheric pressure at room temperature. Exposure of the rotors to air for 100 days between measurement 3 and measurement 4 increased the ETMAC values by approximately 1 % to 2 % compared to the initial measurement 1. Regarding the relative differences of the ETMAC values for different gases, the behaviour of both rotors for measurements 1 and 4 was similar. Ne had the lowest ETMAC values, while He had consistently higher values than the remaining group of gases CH_4, N_2, Ar and Kr.

6.2.2 ETMAC Values of Polished Rotors After the Vacuum Bake

Vacuum bake in the first cycle (measurement 2) showed similar changes for both rotors. ETMAC for Ne slightly increased to a value close to the values for CH_4, N_2, Ar, and Kr, which remained practically unchanged afterwards. ETMAC for He also went up and the difference from the values for CH_4, N_2, Ar, and Kr increased even further. Vacuum bake of the rotors in the second cycle after exposure to air for 100 days (measurement 5) surprisingly showed changes of ETMAC for Ne and He in the opposite direction so that the ETMAC for both gases was lower than the remaining group of gases CH_4, N_2, Ar, and Kr. In addition, the behaviour of rotor A and B was slightly different for CH_4, N_2, Ar and Kr. Average ETMAC value of these gases for rotor A did not change, while for rotor B it decreased by approximately 1 %.

6.2.3 ETMAC Values of Polished Rotors After the Oxygen Bake

After the oxygen bake, a small decrease of less than 1 % of the mean value of the ETMAC of the group of gases CH_4, N_2, Ar, and Kr was observed in both measurement series. However, baking of the polished rotors in oxygen at partial pressure 10^{-2} Pa caused a significant change of the ETMAC for He and Ne in the first measurement series (measurement 3), but the change was smaller after air exposure (measurement 5). In both measurement series, the ETMACs for He and Ne after the oxygen bake were shifted very close together, within

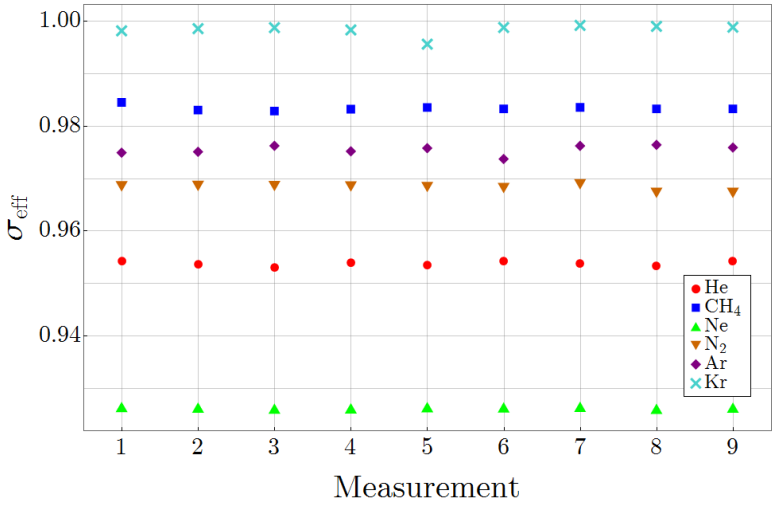

Figure 6.4: ETMAC of the rotor C, used as control, remained constant throughout the experiment. While some deviation occurred for some points, this deviation was not consistent for all six gases, and is therefore expected to be a consequence of insufficient gas purity. The results show good stability of the static expansion method.

0.3 %, and the values were 2 % to 3 % below the mean value of ETMAC for CH_4, N_2, Ar, and Kr.

Conclusions about the Two Measurement Series with the Polished Rotor Surface

Changes of the ETMAC after the vacuum and oxygen bake in the second measurement series showed similar trends for all gases, but the values were not very repeatable. Notably, the mean ETMAC value was lowered after oxygen baking in both cycles (comparing the reductions from measurement 2 to 3, and from 5 to 6). As was the case with the stainless-steel tube, He and Ne are the most sensitive to a surface treatment. Neglecting these two gases, the ETMAC values were comparable for each of the two rotors A and B; the relative difference between ETMAC values was below 0.6 % for each measurement.

The low repeatability of the two cycles (1-3 and 4-6) can be attributed to different initial conditions (measurements 1 and 4). Rotors already received severe treatment during the first measurement cycle, where during the vacuum and oxygen bake the surface was additionally cleaned from the adsorbed layers which could act as corrosion protection of 100Cr6 steel during prolonged exposure to humid laboratory air. We have seen in our laboratory macroscopic rust spots on some rotors which were previously used in vacuum and then left in laboratory air for several months, while we on no occasions saw such things on unused and uncleaned balls that have been kept in the lab in air for more than 10 years.

The relative change of the root-mean-square roughness S_q, calculated from values in Table 6.2, after baking was 25 %. The position of the most probable inclination (Figure 6.6) changed from approximately 2.5° to 4.6°. This change, however, did not greatly affect the ETMAC.

6.2.4 ETMAC Values of the Etched Rotor

The ETMAC values on the etched surface were higher (around 10 %) than on a polished surface, consistent with an increased surface roughness, revealed in SEM images (Fig-

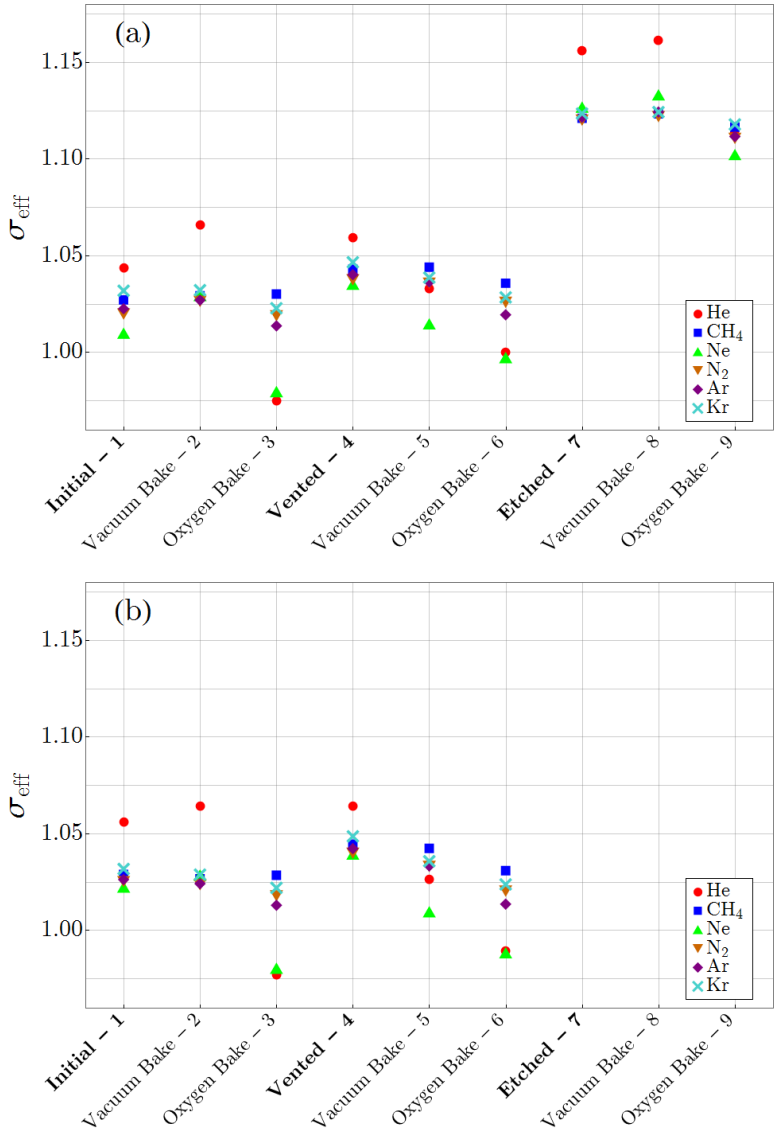

Figure 6.5: ETMAC values after each treatment step described in Section 6.1. Results are shown for rotor A (a) and rotor B (b).

ure 6.1). Large values persisted even after further surface treatment (vacuum and oxygen bake). Contrary to the polished surface, however, the ETMAC changed very little after vacuum baking (change from measurement 7 to 8), with the largest change occurring for He and Ne (0.52 % and 0.53 %, respectively). For other gases, the ETMAC changed by less than 0.2 %. As in the case of the polished rotors, the ETMAC for He was a few percent higher than for all the other gases. The oxygen bake also caused a decrease of the ETMAC for all gases, where a significant decrease of the ETMAC for He, and also a notable decrease for Ne was observed, while the ETMAC of the other gases reduced only slightly. In conclusion, also for the etched surface we observed after vacuum and oxygen bake similar trends for different gases, only the absolute values of the ETMAC were significantly higher.

Root-mean-square roughness S_q of the etched rotor was more than seven times higher than that of the polished rotor and the most probable inclination changed from approximately 2.5° to 17.0°.

Table 6.3: ETMAC values for rotor A prior to etching and rotor B.

	ETMAC					
	Rotor A					
Gas	Initial (1)	Vacuum bake (2)	Oxygen bake (3)	Exposure to air (4)	Vacuum bake (5)	Oxygen bake (6)
He	1.044	1.066	0.975	1.059	1.033	1.000
CH_4	1.027	1.029	1.030	1.043	1.044	1.036
Ne	1.010	1.029	0.980	1.035	1.015	0.997
N_2	1.020	1.026	1.019	1.037	1.036	1.026
Ar	1.022	1.027	1.014	1.040	1.036	1.019
Kr	1.032	1.032	1.023	1.047	1.039	1.028
	Rotor B					
He	1.056	1.064	0.977	1.064	1.026	0.989
CH_4	1.029	1.027	1.029	1.045	1.042	1.031
Ne	1.022	1.029	0.980	1.039	1.010	0.988
N_2	1.025	1.023	1.018	1.040	1.033	1.020
Ar	1.026	1.024	1.013	1.042	1.033	1.014
Kr	1.032	1.029	1.022	1.049	1.036	1.024

Table 6.4: ETMAC values for rotor A after etching.

	ETMAC		
	Rotor A		
Gas	Etched (7)	Vacuum bake (8)	Oxygen bake (9)
He	1.156	1.162	1.113
CH_4	1.121	1.123	1.116
Ne	1.127	1.133	1.102
N_2	1.120	1.122	1.111
Ar	1.122	1.124	1.112
Kr	1.123	1.124	1.118

6.2.5 Gas Dependence of the ETMAC Values

In addition to increasing the ETMAC values, etching was shown to influence the gas dependence of the ETMAC. Variation of the ETMAC values between different gases is shown in Figure 6.7 for rotors A (a) and B (b), presented as the relative difference from the ETMAC value for N_2. Baking a polished surface (both in vacuum and in oxygen, measurements 2 and 3, and 5 and 6) provided no overall benefit to the gas dependence of the ETMAC, due to large fluctuations in the values for the lightest gases He and Ne. However, a different scenario is revealed if He and Ne are excluded. Vacuum baking in the first cycle (measurement 2) shows a decrease in gas dependence of the ETMAC for both rotors. This decrease, however, occurred only in the first cycle, whereas the second cycle (measurement 5) shows no such decrease in either rotor. Further baking in oxygen even nullified this decrease in all cases (measurements 3 and 6 for both rotors).

A different scenario was revealed for the etched surface in Figure 6.7 (a), where variation of the ETMAC values is shown for the rotor A after etching. If all gases are considered,

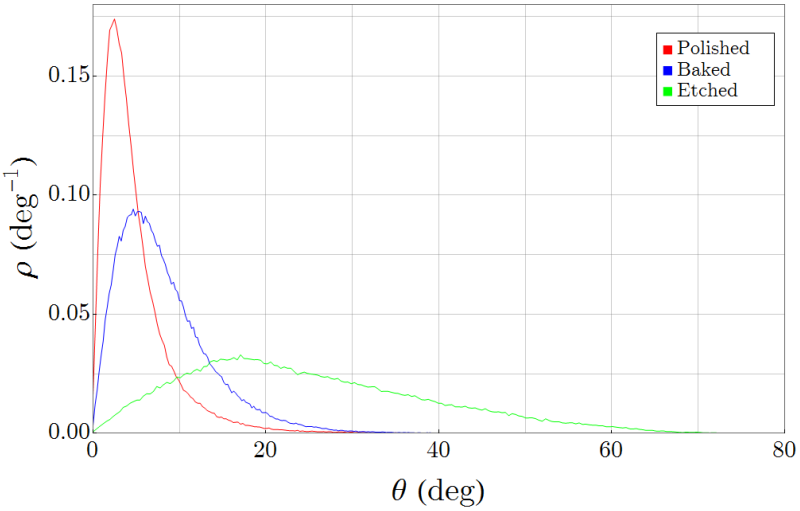

Figure 6.6: Inclination probability distribution of the polished surface, surface after oxygen bake, and etched surface of the SRG rotors. Results were calculated from AFM images.

a vacuum bake of the roughened rotor (measurement 8) shows no decrease in the variation of the ETMAC values, again due to large fluctuations of the ETMAC values for He and Ne. However, if these two gases are excluded, the etched rotor shows a much lower gas dependence (below 0.5 %) directly after etching (measurement 7). Such a low gas dependence persisted even after the vacuum bake (measurement 8). Baking in oxygen, however, resulted in an increased variation, as was the case with polished rotors. Roughening of the surface via an acid etching therefore resulted in the lowest spread of the ETMAC values, where for many practical uses the calibration for a single gas (N_2) would be sufficient also for use in other gases. However, a separate SRG calibration is still necessary for lighter gases, such as Ne and He, if a measurement uncertainty below 1 % is required.

6.3 Comparison of the Rotors and the Tube

Relative changes of the ETMAC for polished surfaces from the initial values to after the exposure to air are shown in Table 6.5. The same is shown for the stainless-steel tube used in Chapter 5, where available. The relative difference for the SRG rotors after re-exposure

Table 6.5: Relative difference in measured ETMAC values of polished rotors A and B between initial values (measurement 1) and values after prolonged exposure to the atmosphere (measurement 4). For comparison, the changes for the electropolished surface of the tube discussed in Chapter 5, where available, are included at the bottom.

	ΔETMAC (%)					
	He	CH_4	Ne	N_2	Ar	Kr
Rotor A	1.50	1.55	2.51	1.73	1.72	1.43
Rotor B	0.78	1.52	1.67	1.43	1.57	1.63
Polished Tube	2.75	/	/	0.14	-0.17	/

to the air was comparable for all the gases, where the maximum change occurred in Ne on the rotor A (2.51 %). He, however, did not exhibit changes significantly larger than the other gases, as was the case for the tube (2.75 % change). Apart from He, changes

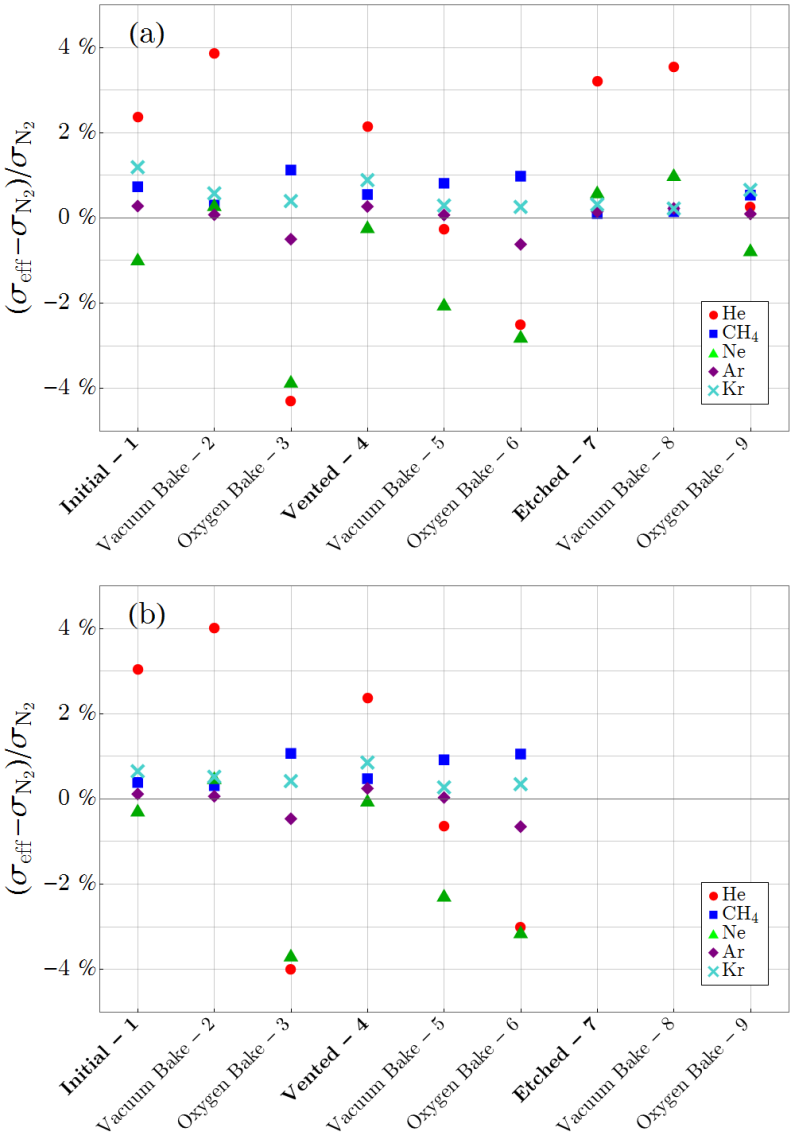

Figure 6.7: Relative difference of ETMAC from the value for N_2 after each treatment step. Results are shown for rotors A (a) and B (b).

in the ETMAC values of the polished rotors were consistently larger than those of the stainless-steel tube.

The different behaviour of the rotors and the tube are probably due to different durations of exposure to air between cycles, where the rotors were exposed to air for three months, but the tube was exposed for only 24 hours. Such a long exposure of the rotors was necessary due to the conflicting schedules of the experiments on the system. Between measurement 3 and 4, the laboratory comparison Euramet.M.P-K15.1 was performed. A possible consequence of the long exposure of clean rotors was surface corrosion (the rotor spheres are made of chrome steel, which is prone to rust). The rotors were visually inspected under a microscope before starting the second cycle, however, and showed no apparent corrosion, but the possibility of corrosion on a microscale cannot be excluded. This possibly led to different initial conditions of the SRG rotors in measurements 1 and 4.

We had a different situation with the stainless-steel tube, where a chromium-rich corrosion protection layer is formed on the stainless-steel surface, and much more repeatable initial conditions on the surface after re-exposure to the atmosphere are established.

For a clearer comparison of the rotors and the tube, Figures 5.4 and 6.5 (a) are again shown in Figure 6.8. In both cases roughening of the surface led to an increase in the

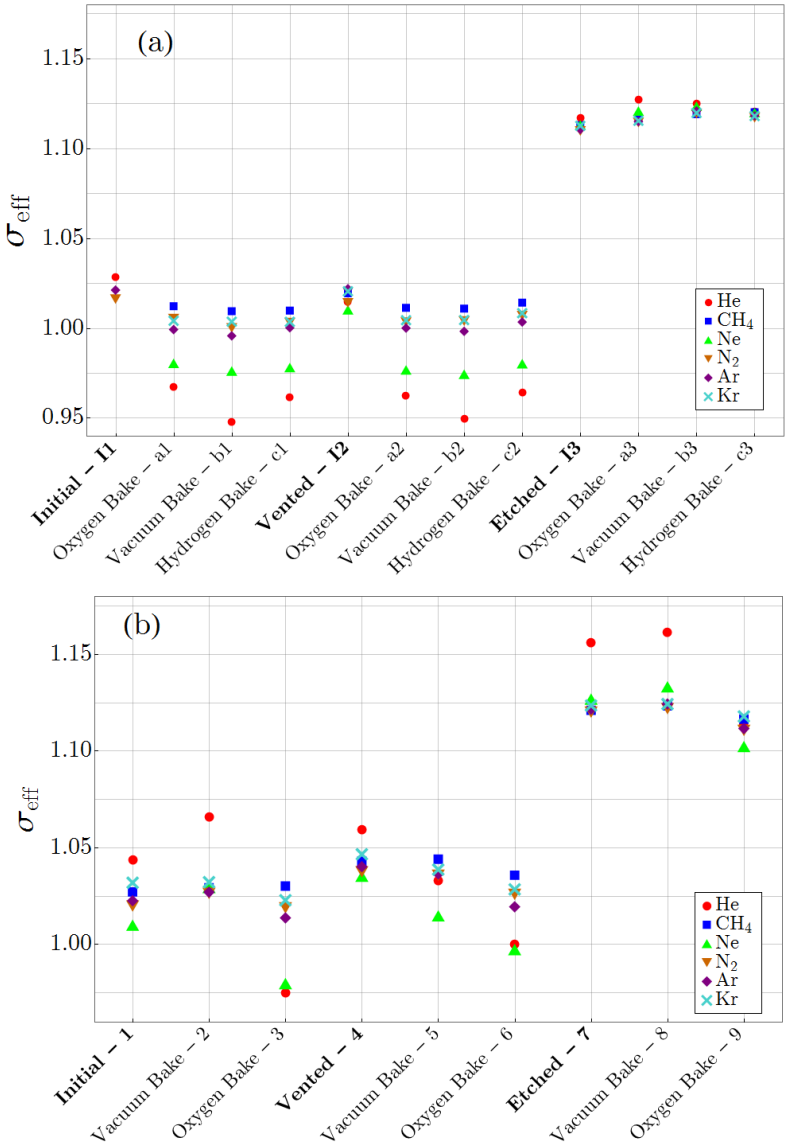

Figure 6.8: Comparison of ETMAC values of the stainless steel tube from Chapter 5 (a) and SRG rotor A from Chapter 6 (b).

ETMAC values by about 10 %. As for gas dependence, the behaviours of both cases are very different. Variations of the ETMAC values for all the gases were much lower for the stainless-steel tube. While for the SRG rotor He and Ne strongly deviated from other gases, this was not the case for the tube.

The different behaviour is presumably a consequence of the different materials of the tube and the rotor. The tube was made of 316-L stainless steel, and the rotors were made out of 100Cr6 chrome steel. These materials react differently to acid etching, as seen in the SEM and AFM images in Figure 5.1 (b) and Figure 5.2 (b) for the tube and

Figure 6.1 (c) and Figure 6.2 (c) for the rotor. Stainless steel showed a very uniformly etched surface. Chrome steel, on the other hand, revealed a large number of flat plateaus. Presumably, these are the carbides present in the chrome steel, which are much more resistant to acid etching. As was discussed in Section 1.2, there are two aspects which determine the ETMAC. The first is the gas-surface interaction. This physical interaction strongly depends on the gas species. The other aspect is the roughness of the surface. On a rough surface the direction in which a gas molecule is scattered depends on the angles of micro-areas on the surface, and does not depend very much on the gas species. Gas dependence on flat surfaces should therefore be much more pronounced than on a rough surface. Therefore, due to the appearance of flat plateaus found on the surface of the etched chrome steel, the gas dependence of the ETMAC should be stronger than on the surface of stainless steel, where there are no flat micro-areas. This consideration supports our findings in this work.

Chapter 7

Conclusions

The aim to minimize measurement uncertainty is common to all fields of experimental research. In vacuum science and metrology, specifically, accurate and precise measurements of pressure are the foundation upon which scientific experiments can be made, and a low measurement uncertainty is therefore necessary. One of the phenomena which demands more research is momentum accommodation on technical surfaces, since the interaction between the gas molecules and surfaces of vacuum systems influences the dynamics of gas flow and molecular drag on the surface. In this thesis we studied two phenomena where momentum accommodation plays an important part: the flow of rarefied gases and the calibration of spinning rotor gauges (SRGs), where the focus was on the effect the surface condition has on momentum accommodation.

Its excellent characteristics in the pressure range from 10^{-4} Pa to 1 Pa enabled us to use the SRG for both experiments. First, however, a study of its measurement uncertainty had to be made. We showed the importance of choosing the appropriate sampling interval and rotor frequency in order to minimize the measurement uncertainty of the SRG. Since a longer sampling interval increases the time required for pressure readings, increasing the rotor frequency is recommended when shorter sampling intervals are desired. By working at a-two-times-higher rotor frequency, the type A measurement uncertainty showed a nearly tenfold decrease. Additionally, the measurement uncertainty can be decreased by increasing the amplitude of the induced voltage signal and, in turn, its slope at zero voltage. Since measurement uncertainty was shown to be inversely proportional to this slope, this can further improve the characteristics of the SRG. The amplitude of the signal level is changed when the rotor is re-suspended in a new magnetic orientation. This can be achieved by removing the SRG measuring head, rolling the rotor across its housing thimble, and replacing the measuring head, which leads to a different orientation of the rotor after re-suspension is established. Changes of amplitude of the signal after such procedure are random and it may be necessary to repeat it few times until a sufficiently high amplitude is achieved.

The effect of momentum accommodation on the flow of rarefied gases was studied in the case of the gas-flow conductance of a long stainless-steel tube using six different pure gases. In order to accurately measure the conductance, the pressure-decay method was implemented using only one SRG for the pressure measurement. Because of how the practical measurement setup was designed and realized, calibration of the SRG was unnecessary, and the measurement uncertainty of this method was below 0.5 %. This high-precision measurement method enabled the detection of small changes in conductance after different heat treatments, which influences the atomic cleanliness of the surface. Changes of the conductance were related to the changes of the effective tangential momentum-accommodation coefficient (ETMAC) of gas molecules on the surface. Heating of the

tube at 573 K in pure oxygen at a low pressure of 0.1 Pa decreased the ETMAC of the electropolished inner surface, most notably with He and Ne (about 5 %). The changes were larger overall for the noble gases compared to the polyatomic gases (CH_4 and N_2), where the changes were below 1.5 %. After subsequent heating in vacuum and in hydrogen at a low pressure of 0.1 Pa, no significant subsequent changes were observed. Roughening the surface by acid etching, on the other hand, increased the ETMAC by about 10 % for all the gases due to the significantly increased surface roughness. Further variations of the ETMAC of the etched surface after heating in oxygen, vacuum and hydrogen were less than 1.1 %, compared to the initial state before the heat treatment. We can conclude that the increased slope of the surface roughness on the etched surface is the main reason for the increase of the ETMAC and the reduction of the measured tube conductance.

Similar surface treatments were made on different SRG rotors, albeit under slightly different conditions. In order to determine the ETMAC of the rotors, the SRGs were calibrated using the primary static expansion method, which is under development in the laboratory for pressure metrology at IMT. A new practical procedure for generating successive calibration pressure values in increasing sequence was introduced. It is based on accumulating an expanded calibration gas without intermediate evacuation of the large calibration volume. This significantly reduces the time needed for the calibration. To the best of our knowledge this procedure is new in the application of primary static gas expansion. Analysis of the uncertainty of our method showed only a slight increase of the uncertainty of the calibration pressure after 10 successive expansions from 0.1 Pa to 1 Pa in steps of 0.1 Pa in our system. The expanded uncertainty of the ETMAC values of the SRG rotors, obtained in this way, was below 0.2 %. This enabled the detection of small changes of the ETMAC values after different surface treatments.

Modifying the surface of the polished rotors by baking ina vacuum and baking in pure oxygen resulted in changes of the ETMAC of up to 8 % for the lightest noble gases (He and Ne), but only up to 2 % for the other gases (CH_4, N_2, Ar, and Kr). The ETMAC of the rotors whose surface was roughened by acid etching was about 10 % higher than that of the polished rotors. Further changes to the surface by baking in a vacuum and in pure oxygen resulted in ETMAC changes of up to 4 % for He, while the change of the ETMAC for other gases is lower.

The main motivation behind this work was to minimize the variation of the ETMAC for different gases. If a surface treatment can be found, which shows little variation, calibration would then not be necessary for every gas used in the application. Furthermore, gas mixtures could be used with minimal measurement uncertainty. Contrary to previously published results [23], we found that roughening the surface of the SRG rotors by acid etching provided a small decrease in the variation of the ETMAC values, and the largest deviation was again found with He and Ne. If these two gases are excluded from the calculation, etching can result in an about two-times-lower spread of the ETMAC values, compared to the polished surface. For the case of the stainless-steel tube, however, the decrease in the ETMAC variation is much larger after acid etching, from around 5 % down to below 1 % for all the gases used (including He and Ne). The difference of our results obtained for the tube and the rotors can be attributed to the fact that the composition of these materials is different. This is also supported by the SEM images of these surfaces. We can then conclude that in applications where various gases are used, roughening the surface by acid etching is a way of reducing variations of the ETMAC for different gases. The largest deviations from the average ETMAC values occur for lightest noble gases: He and Ne.

References

[1] F. Sharipov and O. B. Malyshev, *Vacuum*, vol. 86, no. 11, pp. 1643–1782, May 2012.

[2] ——, *Vacuum*, vol. 109, pp. 1–424, Nov. 2014.

[3] ——, *Gas dynamics and its applications to vacuum science and technology*. Vacuum, 2018.

[4] K. Jousten, *Handbook of vacuum technology*. Weinheim: John Wiley & Sons, 2008.

[5] D. H. Davis, L. L. Levenson, and N. Milleron, "Effect of"rougher-than-rough"surfaces on molecular flow through short ducts," *Journal of Applied Physics*, vol. 35, no. 3, pp. 529–532, 1964.

[6] O. V. Sazhin, S. F. Borisov, and F. Sharipov, "Accommodation coefficient of tangential momentum on atomically clean and contaminated surfaces," *Journal of Vacuum Science & Technology A: Vacuum, Surfaces, and Films*, vol. 19, no. 5, pp. 2499–2503, Sep. 2001, ISSN: 0734-2101. DOI: 10.1116/1.1388622.

[7] T. Verbovšek, B. Š. Batič, and J. Šetina, "Investigation into the influence of surface conditions on the tube conductance for the molecular flow regime," *Vacuum*, vol. 161, pp. 150–156, Mar. 2019, ISSN: 0042-207X. DOI: 10.1016/J.VACUUM.2018.12.040.

[8] M. Knudsen, "The law of molecular flow and viscosity of gases moving through tubes," *Annalen der Physik*, vol. 28, p. 75, 1909.

[9] B. Porodnov, P. Suetin, S. Borisov, and V. Akinshin, "Experimental investigation of rarefied gas flow in different channels," *Journal of Fluid Mechanics*, vol. 64, no. 03, pp. 417–438, 1974.

[10] H. Shinagawa, H. Setyawan, T. Asai, Y. Sugiyama, and K. Okuyama, "An experimental and theoretical investigation of rarefied gas flow through circular tube of finite length," *Chemical engineering science*, vol. 57, no. 19, pp. 4027–4036, 2002.

[11] S. Gimelshein, G. Markelov, T. C. Lilly, N. Selden, and A. Ketsdever, "Experimental and numerical modeling of rarefied gas flows through orifices and short tubes," in *AIP Conference Proceedings*, American Institute of Physics, vol. 762, 2005, pp. 437–443.

[12] H. Yoshida, M. Shiro, K. Arai, M. Hirata, and H. Akimichi, "Effect of surface material and roughness on conductance of channel between parallel disks at molecular flow," *Journal of Vacuum Science & Technology A: Vacuum, Surfaces, and Films*, vol. 28, no. 4, pp. 937–941, 2010.

[13] L. Lund and A. Berman, "Flow and self-diffusion of gases in capillaries. part i," *Journal of applied physics*, vol. 37, no. 6, pp. 2489–2495, 1966.

[14] ——, "Flow and self-diffusion of gases in capillaries. part ii," *Journal of applied physics*, vol. 37, no. 6, pp. 2496–2508, 1966.

[15] J. Maxwell, *The Scientific Papers of James Clark Maxwell*. New York: Dover, 1890.

[16] W. Gaede, "Die äußere Reibung der Gase," *Annalen der Physik*, vol. 346, no. 7, pp. 289–336, Jan. 1913, ISSN: 00033804. DOI: 10.1002/andp.19133460706.

[17] A. S. Berman and W. J. Maegley, "Internal Rarefied Gas Flows with Backscattering," *Physics of Fluids*, vol. 15, no. 5, p. 772, Aug. 1972, ISSN: 00319171. DOI: 10.1063/1.1693983.

[18] W. Sugiyama, T.-i. Sawada, and K. Nakamori, "Rarefied gas flow between two flat plates with two dimensional surface roughness," *Vacuum*, vol. 47, no. 6-8, pp. 791–794, Jun. 1996, ISSN: 0042-207X. DOI: 10.1016/0042-207X(96)00068-1.

[19] F. Sharipov and V. Seleznev, "Data on internal rarefied gas flows," *Journal of Physical and Chemical Reference Data*, vol. 27, no. 3, pp. 657–706, 1998.

[20] O. Sazhin, "The effect of surface roughness on internal free molecular gas flow," *Vacuum*, vol. 159, pp. 287–292, Jan. 2019, ISSN: 0042207X. DOI: 10.1016/j.vacuum.2018.09.031.

[21] A. Agrawal and S. Prabhu, "Survey on measurement of tangential momentum accommodation coefficient," *Journal of Vacuum Science & Technology A: Vacuum, Surfaces, and Films*, vol. 26, no. 4, pp. 634–645, 2008.

[22] J. Fremerey, "Spinning rotor vacuum gauges," *Vacuum*, vol. 32, no. 10-11, pp. 685–690, 1982.

[23] G. Comsa, J. Fremerey, and B. Lindenau, "Tangential momentum transfer in spinning rotor molecular gauges," in *Proceedings of the 7th International Vacuum Congress and the 3rd International Conference on Solid Surfaces*, Vienna, 1977, p. 160.

[24] G. Comsa, J. Fremerey, B. Lindenau, G. Messer, and P. Röhl, "Calibration of a spinning rotor gas friction gauge against a fundamental vacuum pressure standard," *Journal of Vacuum Science & Technology*, vol. 17, no. 2, pp. 642–644, 1980.

[25] K. McCulloh, "Calibration of molecular drag vacuum gages," *Journal of Vacuum Science & Technology A: Vacuum, Surfaces, and Films*, vol. 1, no. 2, pp. 168–171, 1983.

[26] S. Dittmann, B. E. Lindenau, and C. Tilford, "The molecular drag gauge as a calibration standard," *Journal of Vacuum Science & Technology A: Vacuum, Surfaces, and Films*, vol. 7, no. 6, pp. 3356–3360, 1989.

[27] J. Fremerey, "The spinning rotor gauge," *Journal of Vacuum Science & Technology A: Vacuum, Surfaces, and Films*, vol. 3, no. 3, pp. 1715–1720, 1985.

[28] S.-H. Choi, S. Dittmann, and C. R. Tilford, "Stabilization techniques for spinning rotor gage residual drag," *Journal of Vacuum Science & Technology A: Vacuum, Surfaces, and Films*, vol. 8, no. 6, pp. 4079–4085, 1990.

[29] J. Looney, F. Long, D. Browning, and C. Tilford, "PC-based spinning rotor gage controller," *Review of scientific instruments*, vol. 65, no. 9, pp. 3012–3019, 1994.

[30] M. Hirata, H. Isogai, and M. Ono, "Effect of measuring conditions on the accuracy of a spinning rotor gauge," *Journal of Vacuum Science & Technology A: Vacuum, Surfaces, and Films*, vol. 4, no. 3, pp. 1724–1727, 1986.

[31] H. Isogai, "An analysis of the effects of eddy currents on the accuracy of a spinning rotor gauge," *Vacuum*, vol. 48, no. 2, pp. 175–179, 1997.

[32] J. Šetina, "The effect of housing tubes on the zero stability of spinning rotor gauges," *Vacuum*, vol. 41, no. 7-9, pp. 2115–2117, Jan. 1990, ISSN: 0042-207X. DOI: 10.1016/0042-207X(90)94194-U.

[33] J. Setina, "Measurements of spinning rotor gauge response to step change of suspension head temperature," *Vacuum*, vol. 71, no. 1-2, pp. 341–346, 2003.

[34] J. Setina and J. Looney, "Behavior of commercial spinning rotor gages in the transition regime," *Vacuum*, vol. 44, no. 5-7, pp. 577–580, 1993.

[35] B. Lindenau and J. Fremerey, "Linearization and temperature compensation up to one atmosphere for the spinning rotor gauge," *Journal of Vacuum Science & Technology A: Vacuum, Surfaces, and Films*, vol. 9, no. 5, pp. 2737–2743, 1991.

[36] J. Šetina, "Two point calibration scheme for the linearization of the spinning rotor gauge at transition regime pressures," *Journal of Vacuum Science & Technology A: Vacuum, Surfaces, and Films*, vol. 17, no. 4, pp. 2086–2092, 1999.

[37] EA Laboratory Committee and others, "Evaluation of the uncertainty of measurement in calibration," European co-operation for Accreditation, 2013.

[38] R. F. Berg and J. A. Fedchak, "Nist calibration services for spinning rotor gauge calibrations," *NIST Special Publication*, vol. 250, p. 93, 2015.

[39] R. F. Chang and P. J. Abbott, "Factors affecting the reproducibility of the accommodation coefficient of the spinning rotor gauge," *Journal of Vacuum Science & Technology A: Vacuum, Surfaces, and Films*, vol. 25, no. 6, pp. 1567–1576, 2007.

[40] G. Messer, P. Röhl, G. Grosse, and W. Jitschin, "High vacuum measured by the spinning rotor gauge: Status report of the bureau international des poids et mesures intercomparison," *Journal of Vacuum Science & Technology A: Vacuum, Surfaces, and Films*, vol. 5, no. 4, pp. 2440–2443, 1987.

[41] P. Richter, "Estimating errors in least-squares fitting," *The Telecommunications and Data Acquisition Progress Report 42-122*, p. 107, 1995.

[42] A. Berman and J. K. Fremerey, "Precision calibration of a static pressure divider by means of a spinning rotor gauge," *Journal of Vacuum Science & Technology A: Vacuum, Surfaces, and Films*, vol. 5, no. 4, pp. 2436–2439, Jul. 1987, ISSN: 0734-2101. DOI: 10.1116/1.574865.

[43] J. Setina, S. Avdiaj, and B. Erjavec, "Measuring volume ratios of vacuum vessels using non-evaporable getters," *Vacuum*, vol. 92, pp. 20–25, Jun. 2013, ISSN: 0042-207X. DOI: 10.1016/J.VACUUM.2012.11.010.

[44] J. Gómez-Goñi and P. J. Lobo, "Comparison between Monte Carlo and analytical calculation of the conductance of cylindrical and conical tubes," *Journal of Vacuum Science & Technology A: Vacuum, Surfaces, and Films*, vol. 21, no. 4, pp. 1452–1457, Jul. 2003, ISSN: 0734-2101. DOI: 10.1116/1.1568746.

Bibliography

Publications Related to the Thesis

Journal Articles

T. Verbovšek, B. Š. Batič, and J. Šetina, "Investigation into the influence of surface conditions on the tube conductance for the molecular flow regime," *Vacuum*, vol. 161, pp. 150–156, Mar. 2019, ISSN: 0042-207X. DOI: 10.1016/J.VACUUM.2018.12.040.

Invited Lectures Related to the Thesis

T. Verbovšek, "Measuring the effect of surface conditions on gas flow conductance," in *25th International Scientific Meeting on Vacuum Science and Technique*, Gozd Martuljek, Slovenia: Slovenian Society for Vacuum Technique, 2018.

Other Publications

Journal Articles

T. Verbovšek, B. Š. Batič, J. Šetina, and T. Kokalj, "A capillary manometer for pressure measurements in small cavities," *Vacuum*, vol. 138, pp. 178–183, 2017.

B. Š. Batič, T. Verbovšek, and J. Šetina, "Decomposition of thin Au films on flat and structured Si substrate by annealing," *Vacuum*, vol. 138, pp. 134–138, 2017.

Biography

The author of this thesis Tim Verbovšek obtained his Bachelor's degree in physics at the Faculty of Mathematics and Physics, University of Ljubljana, Slovenia in 2012. During this time he joined a research team in the SPM Laboratory at the Jozef Stefan Institute, where his work involved assembly and operation of a scanning tunnelling microscope.

In 2012 he started his Master's studies in Condensed Matter Physics programme at the Faculty of Mathematics and Physics. His work in scanning tunnelling microscopy enabled him to obtain his M.Sc. degree, where the title of his thesis was "Study of a Passive CuN monolayer using STM Microscopy".

From 2015 he was employed as a young researcher at the Institute of Metals and Technology (IMT), at the department of Vacuuum Science and Opto Electronics. During that time he was enrolled in the Nanosciences and Nanotechnologies doctoral studying program at the Jožef Stefan International Postgraduate School (IPS).